The Effect of Defects on Functional Properties of Niobium for Superconducting Radio-

Frequency Cavities: A First-Principles Study

by

Pulkit Garg

A Dissertation Presented in Partial Fulfillment
of the requirements for the Degree
Doctor of Philosophy

Approved September 2019 by the
Graduate Supervisory Committee:

Kiran N. Solanki, Chair
Yang Jiao
Jay Oswald

ARIZONA STATE UNIVERSITY

December 2019

ABSTRACT

Niobium is the primary material for fabricating superconducting radio-frequency (SRF) cavities. However, presence of impurities and defects degrade the superconducting behavior of niobium twofold, first by nucleating non-superconducting phases and second by increasing the residual surface resistance of cavities. In particular, niobium absorbs hydrogen during cavity fabrication and promotes precipitation of non-superconducting niobium hydride phases. Additionally, magnetic flux trapping at defects leads to a normal conducting (non-superconducting) core which increases surface resistance and negatively affects niobium performance for superconducting applications. However, undelaying mechanisms related to hydride formation and dissolution along with defect interaction with magnetic fields is still unclear. Therefore, this dissertation aims to investigate the role of defects and impurities on functional properties of niobium for SRF cavities using first-principles methods.

Here, density functional theory calculations revealed that nitrogen addition suppressed hydrogen absorption interstitially and at grain boundaries, and it also decreased the energetic stability of niobium hydride precipitates present in niobium. Further, hydrogen segregation at the screw dislocation was observed to transform the dislocation core structure and increase the barrier for screw dislocation motion. Valence charge transfer calculations displayed a strong tendency of nitrogen to accumulate charge around itself, thereby decreasing the strength of covalent bonds between niobium and hydrogen leading to a very unstable state for interstitial hydrogen and hydrides. Thus,

i

presence of nitrogen during processing plays a critical role in controlling hydride precipitation and subsequent SRF properties.

First-principles methods were further implemented to gain a theoretical perspective about the experimental observations that lattice defects are effective at trapping magnetic flux in high-purity superconducting niobium. Full-potential linear augmented plane-wave methods were used to analyze the effects of magnetic field on the superconducting state surrounding these defects. A considerable amount of trapped flux was obtained at the dislocation core and grain boundaries which can be attributed to significantly different electronic structure of defects as compared to bulk niobium. Electron redistribution at defects enhances non-paramagnetic effects that perturb superconductivity, resulting in local conditions suitable for flux trapping. Therefore, controlling accumulation or depletion of charge at the defects could mitigate these tendencies and aid in improving superconductive behavior of niobium.

ACKNOWLEDGMENTS

TABLE OF CONTENTS

v

LIST OF TABLES

LIST OF FIGURES

CHAPTER 1

1 MOTIVATION

Niobium is the primary material for manufacturing superconducting radio-frequency (SRF) cavities for many modern high-performance particle accelerators like International Linear collider etc. The selection of the superconductor for SRF applications is based on their operating temperatures requirement, typically in the range 1.8 – 4.2 K, to minimize the surface resistance and provide and sustain high electromagnetic fields to accelerate the charged particles inside the cavities. Niobium has the highest critical temperature (T_c) of all the pure elements (9.25 K), has high critical magnetic fields and is highly malleable as it can be formed into complex shapes; thus, making it a prime candidate for SRF cavities (Ford, Cooley, and Seidman 2013a). Furthermore, niobium has high enough thermal conductivity which also plays a role in reaching high surface fields which can become difficult if the thermal conductivity is too low (Aizaz et al. 2007). However, niobium can readily absorb hydrogen, which may occupy interstitial sites or precipitate into ordered hydride phases, depending on the hydrogen concentration and temperature, significantly affecting its properties (Alefeld and Völkl 1978). Further, the phenomenon of flux trapping at defects and impurities in niobium leads to a non-superconducting core which plays an important role in degrading its performance (Aull, Kugeler, and Knobloch 2012). Thus, a great deal of attention has been dedicated to advance the performance of SRF niobium cavities.

The performance of SRF cavities is measured in terms of the quality factor $Q = G/R_s$, where the geometric factor G depends on the cavity geometry and R_s is the average surface resistance of the inner cavity wall, as a function of the accelerating gradient field (E_{acc}) (Pashupati Dhakal et al. 2015). Typically, Nb cavities have a Q value in the range of 10^{10}–10^{11}. However, the absorbed hydrogen contaminates niobium and severely degrades the cavity Q starting at very low accelerating fields itself thereby making these SRF cavities useless (Knobloch 2003; Barkov et al. 2013). Formation of ordered hydride phases leads to hydrogen embrittlement and also affects the superconducting properties since the hydride phases are not superconducting above 1-2 K (Jisrawi et al. 1998; Isagawa 1980). Furthermore, the SRF cavities operate in the superconducting state but the presence of defects and other imperfections suppress the expulsion of magnetic field and pin the field inside the material even after the external magnetic field is removed. As a result, the trapped flux contributes to a normal conducting core and residual surface resistance and decreases the quality factor (Vallet et al. 1992; Aull, Kugeler, and Knobloch 2012). Therefore, the improvement in quality factor and acceleration gradients of SRF cavities is critical in the development of current and future accelerators. Thus, in the present work, the role of defects on functional properties of niobium for SRF cavities were examined using first-principles methods. The effect of nitrogen doping on hydrogen absorption and stability of hydride precipitate in niobium was investigated through density functional theory calculations. Further, this work marks the first attempt to understand the interaction between external magnetic field and lattice defects, i.e., vacancies, dislocations and grain boundaries in Nb within the first-principles framework.

2

CHAPTER 2

2 LITERATURE REVIEW AND RESEARCH OBJECTIVES

2.1 Literature Review

The presence of hydrogen in niobium leads to an increase of 1-2 orders of magnitude

in surface resistance, thereby causing a proportional decrease in Q. In addition to

interstitial sites, the absorbed hydrogen can readily segregate at lattice defects and grain

boundaries in niobium and lead to hydrogen embrittlement (Myers et al. 1992).

Unfortunately, many opportunities exist for hydrogen to get absorbed in niobium during

fabrication and processing of cavities (Barkov, Romanenko, and Grassellino 2012).

Buffered chemical polishing (BCP) or electropolishing (EP) is one of the possible

processing methods where niobium can get contaminated with hydrogen (Higuchi et al.

2001). Centrifugal barrel polishing (CBP) using water based solution, which is not

hydrogen free, also results in hydrogen contamination (Barkov, Romanenko, and

Grassellino 2012). Hydrogen reabsorption is also possible from the furnace upon

cooldown after baking at 600-800°C (Isagawa 1980; Faber and Schultz 1972). Hydrogen

concentration can be high near surface (~100 nm depth) since hydrogen can get trapped

near the surface due to elastic strains (Lagos, Martinez, and Schuller 1984; Smith 1980;

Cabrera et al. 2002; Romero, Schuller, and Ramirez 1998). The severity of the degrading

effects of hydrogen depends on the hydrogen concentration, cavity processing

temperature and the presence of other impurities and defects in niobium.
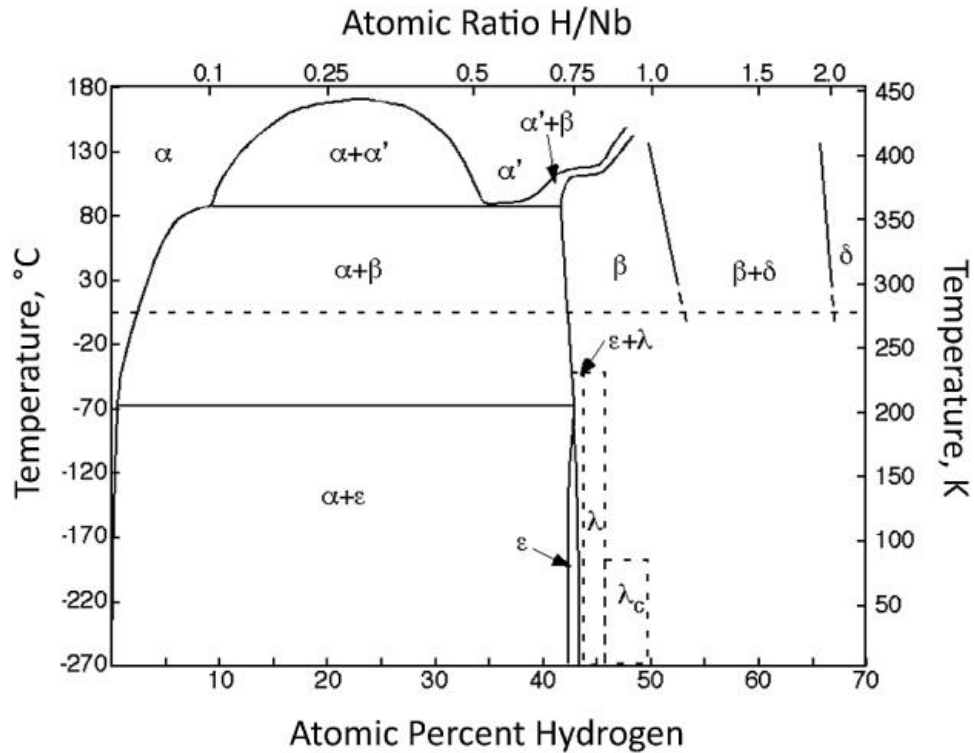
Figure 1: Phase diagram of niobium with different atomic percentages of hydrogen (Ricker and Myneni 2010).

Hydrogen forms different phases with niobium as shown in the niobium hydrogen phase diagram in figure 1. The α and α' are disordered hydride phases which exist at low hydrogen concentrations. In disordered hydride phases, hydrogen is present at the interstitial tetrahedral sites in body centered cubic (BCC) niobium and the phases differ only in the lattice parameter based on hydrogen concentration. Ordered hydride phases occur at higher hydrogen concentration and low temperatures, and consists of β, δ and ε phases(Alefeld and Völkl 1978). β-NbH has an atomic ratio H/Nb = 1, face centered orthorhombic (fco) structure with niobium atoms at lattice sites and hydrogen atoms at interstitial tetrahedral sites. δ-NbH$_2$ has a CaF$_2$ type face centered cubic structure with

4

H/Nb = 2 while ε-Nb$_4$H$_3$ has H/Nb = 3/4 and an orthorhombic structure. The λ phase has an approximate ratio of 0.8 but no structural information is available and not well established yet (Welter and Johnen 1977). It has also been found that multiple hydride phases can exit simultaneously in niobium (Kim et al. 2013).

Many experimental methods like X-ray, neutron and electron diffraction, differential thermal analysis (DTA), resistivity, susceptibility, optical microscopy, and transmission (TEM) and scanning (SEM) electron microscopies have been used to study niobium - hydrogen system for different hydrogen concentrations (Barkov, Romanenko, and Grassellino 2012; Barkov et al. 2013; Trenikhina et al. 2015; Schober, Pick, and Wenzl 1973). Recently, first-principles using density functional theory (DFT) calculations are also being performed to understand the niobium hydrogen interactions (Ford, Zapol, and Cooley 2015).

2.1.1 Hydride Precipitates in Niobium SRF Cavities

Niobium hydride phases have been observed using laser and optical microscopy to understand the effects of hydrides in SRF niobium cavities (Barkov, Romanenko, and Grassellino 2012). Hydrides were observed in mechanically polished fine grain niobium samples while hydrides were absent in chemically polished fine grain samples (EP or BCP) (Barkov, Romanenko, and Grassellino 2012; Barkov et al. 2013). After polishing, all the samples were baked at 800°C for 2 hrs in the vacuum furnace, then quickly cooled down to 140 K and kept at that temperature for 3 hrs to study growth of hydride precipitates. All the hydrides represented ~3 μm high bumps on the surface but their shapes were found to be dependent on the crystallographic orientation of each grain.

After holding the sample at 140 K for 3 hrs, it was further cooled down quickly to ~5 K
and smaller hydride precipitates were observed around ~100 K. These small hydrides
were observed at the grain boundaries (Barkov et al. 2013). High starting concentration
of hydrogen in the single crystal niobium samples leads to the presence of hydride phases
after EP or BCP treatments, indicating the requirement of hydrogen degassing (Barkov et
al. 2013).
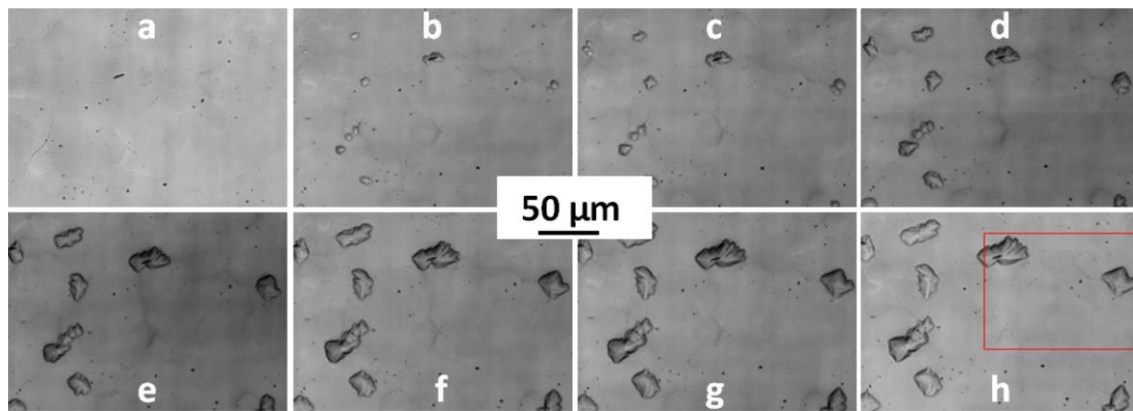
Figure 2: Time evolution of hydride structures observed on a mechanically polished fine
grain sample at 140 K: (a) room temperature; (b) after 60s at 140 K; (c) 120 s; (d) 300 s;
(e) 900 s; (f) 2700 s; (g) 6000 s; (h) 10 800 s. Smaller hydrides were observed in (h)
(Barkov et al. 2013).

Formation of stoichiometric ordered niobium hydrides was studied using temperature
dependent nano-area electron diffraction (NED) and scanning electron nano-area
diffraction (SEND) techniques. SEND map along with TEM image was taken for an
electropolished fine grain niobium (~50 μm) sample at a cryogenic temperature of 94K
(see figure 3). In figure 3(a), each square represents a sample area of diameter equal to
the diameter of the diffraction probe. It was found that ε-Nb_4H_3 (see figure 3b) as well as

β-NbH (see figure 3c) diffraction patterns overlapped with [110] Nb respectively (Trenikhina et al. 2015). Formation of nanoscale niobium hydrides near the surface at low temperatures was seen for the first time using cryogenic NED and SEND techniques (Trenikhina et al. 2015).
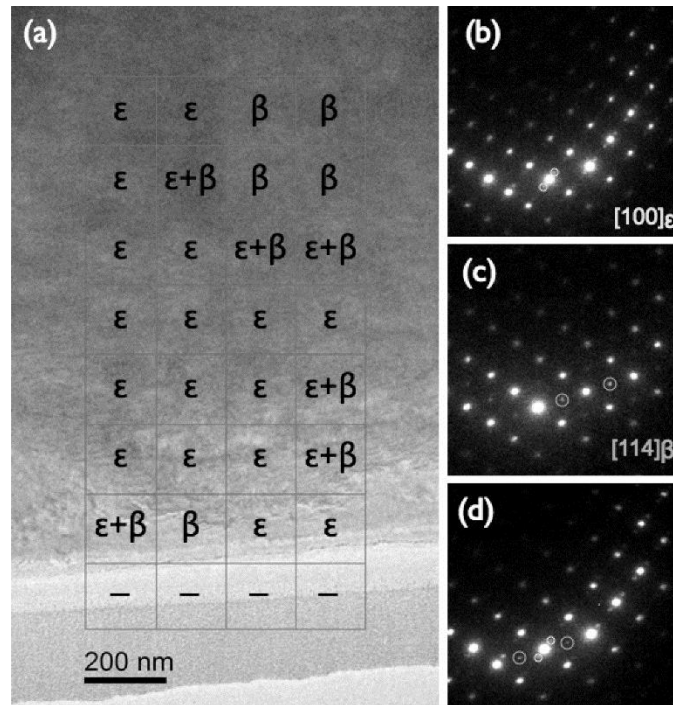
Figure 3: (a) SEND map of EP sample at 94 K using TEM, (b) ε-Nb_4H_3 overlapped with Nb, (c) β-NbH phase overlapped with Nb and (d) ε-Nb_4H_3 and β-NbH overlapped with Nb (Trenikhina et al. 2015).

First principle calculations using density functional theory also show that hydrogen is readily absorbed from gas phase into niobium by releasing 0.28 eV of energy. Hydrogen atoms occupy interstitial tetrahedral sites and expand the crystal lattice. Niobium atoms are displaced from their lattice sites by interstitial hydrogen creating lattice distortions which decrease the structural stability of niobium (Alefeld and Völkl 1978). Furthermore,

7

ordered β–NbH phase is energetically more stable than disordered hydride phase with the same H/Nb atomic ratio of 1. Thus, phase transformation from disordered hydrogen in BCC niobium to ordered β-niobium hydride phase occurs to minimize repulsion between hydrogen atoms and maximize the charge transfer from niobium to hydrogen (Ford, Cooley, and Seidman 2013a).

2.1.2 Nitrogen Doping to Suppress Hydrides in SRF Niobium Cavities

SRF cavities were doped with nitrogen for the first time by Grassellino et. al. in an attempt to lower the surface resistance of SRF niobium cavities (A Grassellino and A Romanenko and D Sergatskov and O Melnychuk and Y Trenikhina and A Crawford and A Rowe and M Wong and T Khabiboulline and F Barkov 2013). Vacuum heat treatment of SRF niobium cavities followed by material removal using electropolishing lowered cavity surface resistance. The measured Q values for the cavity surfaces treated with nitrogen followed by surface removal were significantly higher as compared to the typical Q values for surfaces treated with standard methods (Gonnella and Liepe 2014; Gonnella et al. 2014; Pashupati Dhakal et al. 2015; A Grassellino and A Romanenko and D Sergatskov and O Melnychuk and Y Trenikhina and A Crawford and A Rowe and M Wong and T Khabiboulline and F Barkov 2013). Also, the field dependence of Q reversed and showed an extended anti-Q-slope, contrary to the standard medium Q-slope behavior of SRF niobium cavities (see figure 4) (A Grassellino and A Romanenko and D Sergatskov and O Melnychuk and Y Trenikhina and A Crawford and A Rowe and M Wong and T Khabiboulline and F Barkov 2013).
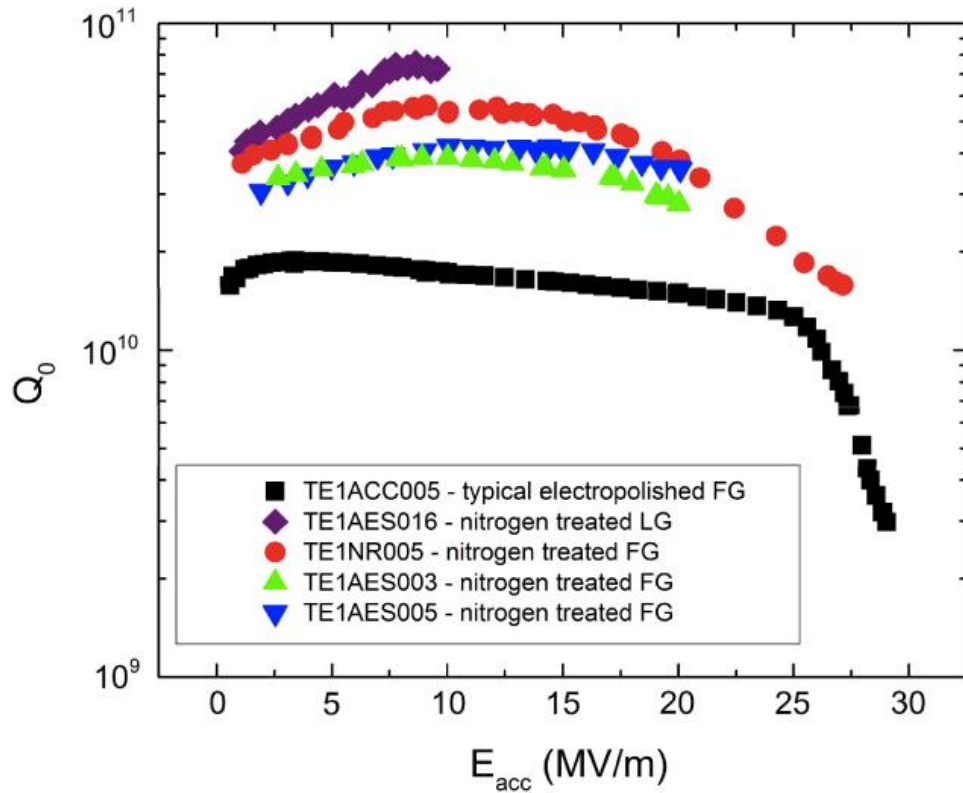
Figure 4: Comparison of quality factors versus accelerating field for nitrogen-treated cavities and standardly adopted treatment (A Grassellino and A Romanenko and D Sergatskov and O Melnychuk and Y Trenikhina and A Crawford and A Rowe and M Wong and T Khabiboulline and F Barkov 2013).

First-principles calculations show that oxygen acts as a trapping site for hydrogen atoms. In niobium, both hydrogen and oxygen have partially anionic character which leads to their repulsive interactions and suppresses hydrogen-hydrogen interactions to inhibit hydride formation. It has also been proposed that oxygen atoms in octahedral sites and oxide layer can migrate to vacancies on the surface and prevent reabsorption of hydrogen at vacancies (Ford, Zapol, and Cooley 2015; Ford, Cooley, and Seidman 2013a). Similar inhibiting effect is expected from interstitial nitrogen atoms, however

9

understanding about the effect of nitrogen on hydrogen absorption and hydride

precipitation in niobium is limited since such calculations have not been performed yet.

2.1.3 Flux Trapping in Superconducting Niobium

Externally applied magnetic field (B_{ext}) is completely expelled from the SRF cavities

as they operate in the Meissner state (see figure 5a). But the presence of defects or other

inhomogeneities like impurities, dislocations and grain boundaries can suppress the

expulsion of magnetic field during the transition to the superconducting state. As a result,

the field can get pinned inside the material even after the external magnetic field is

removed (see figure 5b).

a) Perfect Meissner effect
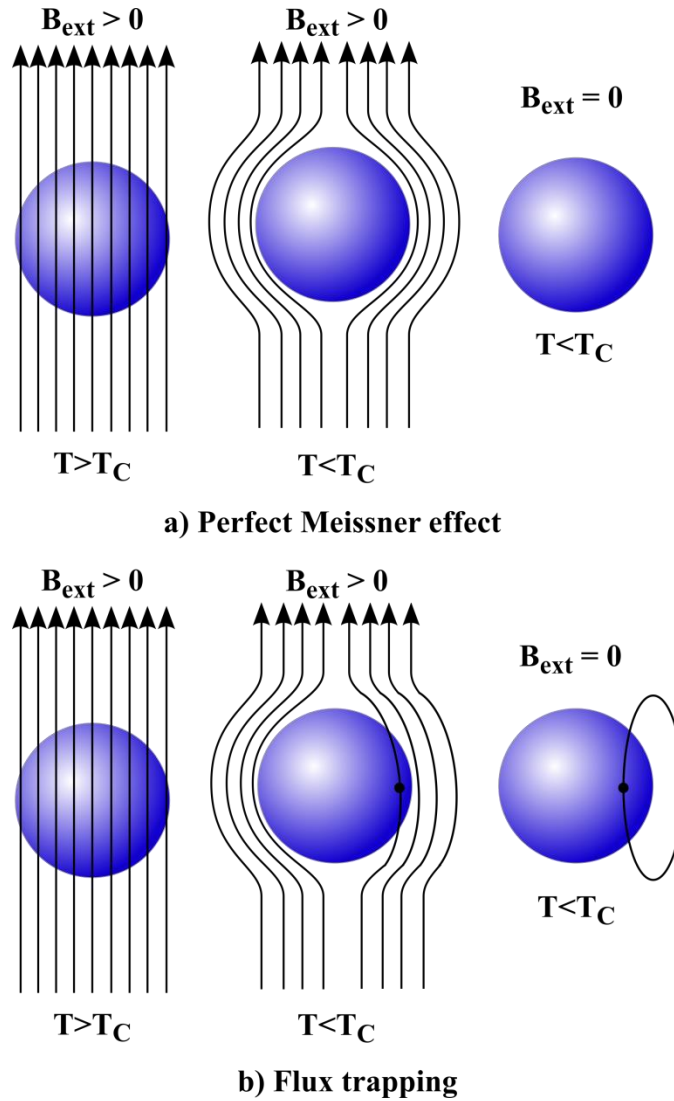
b) Flux trapping

Figure 5: Comparison between the perfect Meissner effect and flux trapping (Aull, Kugeler, and Knobloch 2012). Below T_c (a) the superconductor expels all the applied magnetic field (Meissner state), but (b) due to presence of defects and impurities field is partially expelled and gets pinned inside the material even after the external source is removed.

The flux is trapped mainly at the cavity walls in the form of flux tubes, which have a normal conducting core. The unpaired electrons in the flux containing areas will cause ohmic resistance which contributes to the residual surface resistance and decreases the

quality factor (Aull, Kugeler, and Knobloch 2012; Vallet et al. 1992). Aull et al. (Aull, Kugeler, and Knobloch 2012) measured magnetic flux trapped in different niobium samples to understand the impact of different treatments and operating conditions on flux trapping. Samples 1-3 were polycrystalline with no treatment, with BCP treatment and with BCP treatment followed by 800°C tempering respectively. Samples 4-6 were BCP treated single crystal niobium with no tempering, 800°C tempering and 1200°C tempering respectively. It was found that almost all the applied field was trapped in sample 1 and sample 2 while the amount of trapped flux was less for other samples with minimum trapping for sample 6.
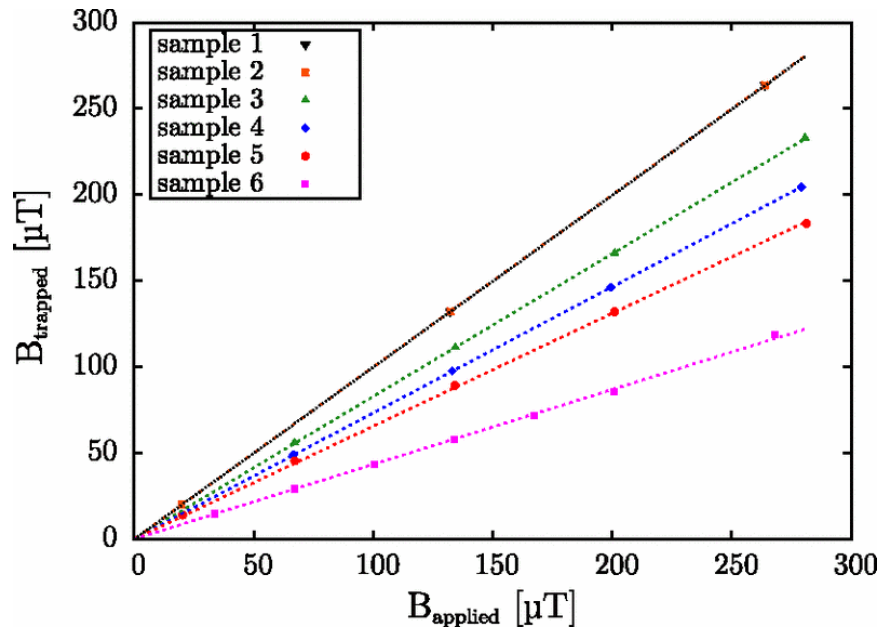
Figure 6: Trapped field vs applied field for all samples with different treatment methods (Aull, Kugeler, and Knobloch 2012).

Many experimental methods have been applied so far to study niobium-hydrogen system for different concentrations of hydrogen, however quantitative evaluation of

12

hydrogen in SRF cavities is difficult and in situ observations have not been possible (Barkov, Romanenko, and Grassellino 2012; Barkov et al. 2013; Schober, Pick, and Wenzl 1973). Experimentally, nitrogen doping has been reported to improve the quality of niobium for SRF cavities but the underlying mechanisms are still unclear (Pashupati Dhakal et al. 2015; A Grassellino and A Romanenko and D Sergatskov and O Melnychuk and Y Trenikhina and A Crawford and A Rowe and M Wong and T Khabiboulline and F Barkov 2013; Gonnella et al. 2014). Furthermore, experimentally, it has been seen that extent flux trapping depends on the concentration of impurities, various defects present and the number of grain boundaries (Aull, Kugeler, and Knobloch 2012) but it has not been possible to determine the contributions of each defect and impurity.

2.2 Research Objectives

The improvement in quality factor of niobium for SRF cavities is critical in the development of current and future accelerators. The two major contributors to the surface resistance and thus Q degradation of niobium are the presence of hydrogen/hydride precipitates and magnetic flux trapping at defects in niobium. Therefore, the objectives of this dissertation aim to address some of the critical questions about the role of defects and impurities on properties of niobium for SRF cavities within the first-principles framework:

1. Understanding the effect of nitrogen doping on hydrogen absorption and hydride precipitates in body centered cubic niobium.

In the last few years the addition of dopant elements such as nitrogen has been experimentally shown to significantly improve the quality factor of niobium SRF

cavities. One of the contributors to Q degradation can be presence of hydrides, however, the underlying mechanisms associated with the kinetics of hydrogen and the thermodynamic stability of hydride precipitates in the presence of dopants are not well known. Using first principles calculations, the effects of nitrogen on the energetic preference for hydrogen to occupy interstitial sites and hydride stability are examined (Chapter 3). In particular, the presence of nitrogen significantly increased the energy barrier for hydrogen diffusion from one tetrahedral site to another interstitial site. Furthermore, the beta niobium hydride precipitate became energetically unstable upon addition of nitrogen in the niobium matrix. These calculations show that the presence of nitrogen during processing plays a critical role in controlling hydride precipitation and subsequent SRF properties.

2. Investigate the effect of hydrogen segregation at dislocation core structure and grain boundaries defects in niobium.

The low temperature plasticity of niobium is primarily controlled by the motion of screw dislocation on the glide plane leading to increase in the yield stress with decreasing temperature. Presence of interstitial impurities like hydrogen can alter the structure and motion of dislocation core therefore significantly affecting the plastic behavior of niobium. Additionally, grain boundaries act as preferential sites for impurity segregation which can lead to intergranular failure at the interface along with degraded superconducting properties. Thus, first-principles calculations were employed to investigate the effect of hydrogen segregation at $1/2 \langle 111 \rangle$ screw dislocation core and $\Sigma 5$ symmetric tilt grain boundaries in Nb (Chapter 4). The screw dislocation core was

observed to transform from a non-degenerate to degenerate dislocation core upon addition of hydrogen. The valence charge transfer calculations indicated towards hydride precipitation as a contributing factor to the stability of degenerate dislocation core configuration upon addition of hydrogen. Further, presence of hydrogen increased the energy barrier for dislocation motion leading to solute hardening and significantly altering the plastic behavior of niobium. Additionally, nitrogen doping significantly affected hydrogen segregation at niobium grain boundaries, however the suppressing effect of nitrogen on hydrogen segregation was dominant only in the proximity of nitrogen, approximately up to 2.6 Å.

3. Assessing the role of different lattice defects and magnetic flux trapping in niobium.

Superconducting niobium operates in Meissner state and therefore expels the external magnetic field; however, the lattice defects pin the field inside the material even after the external field is reduced and thus reduces the effectiveness of niobium. First-principles methods were used (Chapter 5) to gain a theoretical perspective about the experimental observation that vacancies, dislocations, and grain boundaries are effective at trapping magnetic flux in carefully prepared, high-purity superconducting niobium. Full-potential linear augmented plane-wave methods were then used to analyze the effects of magnetic field on these lattice defects. The simulations identified changes in electronic structure at the dislocation core and within different types of symmetric tilt grain boundaries relative to bulk niobium. Further, charge re-redistribution enhanced non-paramagnetic effects that perturb superconductivity, resulting in local conditions suitable for flux trapping and pinning.

15

CHAPTER 3

3 THE EFFECT OF NITROGEN ON HYDROGEN ABSORPTION AND HYDRIDE

PRECIPITATES IN NIOBIUM

3.1 Introduction

Niobium is used for manufacturing SRF cavities because it has both, the highest

lower magnetic field (H_{c1}~190 mT) and the highest superconducting transition

temperature (T_c = 9.25 K) of any element as well as high ductility that enables forming of

complex shapes (Sung et al. 2017; Ford, Cooley, and Seidman 2013a). However,

hydrogen absorbed during chemical processing steps segregate near defects (point, line or

planar defects) or precipitate into hydride phases and degrade performance of niobium (A

Romanenko and L V Goncharova 2011; Hardie and McIntyre 1973; Janisch and Elsässer

2003). Segregation of interstitial hydrogen atoms and hydride precipitation leads to

localized breakdown of surface superconductivity due to proximity coupling during

cavity operation at radio frequencies (Higuchi et al. 2001; Knobloch 2003; Barkov et al.

2013; Jisrawi et al. 1998; Isagawa 1980). Advances in cavity preparation techniques such

as high temperature heat treatments (>600˚C) followed by low temperature baking

(120˚C), diffusion of nitrogen into sub-surface layers of Nb have been developed to

improve the cryogenic efficiency (operation at higher accelerating fields) of current and

future accelerators (Barkov, Romanenko, and Grassellino 2012; Barkov et al. 2013;

Trenikhina et al. 2015; Schober, Pick, and Wenzl 1973; Pashupati Dhakal, Ciovati, and

Myneni 2017). For instance, recent experiments show significantly higher intrinsic

quality factors, for cavity surfaces treated in a nitrogen atmosphere as compared to surfaces with no nitrogen treatment (Gonnella and Liepe 2014; Gonnella et al. 2014; P Dhakal et al. 2013; A Grassellino and A Romanenko and D Sergatskov and O Melnychuk and Y Trenikhina and A Crawford and A Rowe and M Wong and T Khabiboulline and F Barkov 2013; Pashupati Dhakal et al. 2018). Furthermore, the effect of nitrogen on the radio frequency surface resistance and the trapped magnetic flux sensitivity (energy loss mechanisms) has been reported to depend strongly on cavity processing techniques (Gonnella, Kaufman, and Liepe 2016; Martinello et al. 2016). However, many fundamental questions related to the kinetic and thermodynamic aspects of such improvements remain elusive.

In general, the observed improvement in performance of nitrogen doped cavities can be attributed to the reduction of surface resistance (Pashupati Dhakal et al. 2015; Romanenko et al. 2013) and trapping of interstitial hydrogen by nitrogen that prevents hydride nucleation (G Pfeiffer and H Wipf 1976; Romanenko et al. 2013). Hydride formation leads to plastic distortions in the niobium lattice, which helps to easily observe the (Barkov, Romanenko, and Grassellino 2012) hydride pits ex-situ due to strain contrast in back scatter electron imaging under a microscope. Hydride formation in niobium wires that underwent cavity relevant heat treatments, including a traditional 800°C/3 h heat treatment (control), versus nitrogen doping/diffusion heat treatment was compared. The nitrogen treatment involved, 800°C/3h heat treatment in vacuum followed by a two minute flow of N_2 gas at a partial pressure of 5 mTorr after which the N_2 supply was shut, and the sample was soaked at 800°C for six minutes. This recipe is commonly referred to

as "8002N6" in the SRF community (A Grassellino and A Romanenko and D Sergatskov and O Melnychuk and Y Trenikhina and A Crawford and A Rowe and M Wong and T Khabiboulline and F Barkov 2013). The 8002N6 recipe with nitrogen diffusion through the surface of the wire show low hydride pit concentration in regions where nitrogen concentration is higher (Figure 7a and 7b) (Balachandran et al. 2017). Within the first 50 μm from the surface, a 60% decrease in the density of hydrides was observed in the niobium coupons treated in a nitrogen atmosphere compared to the control sample (Figure 7c).
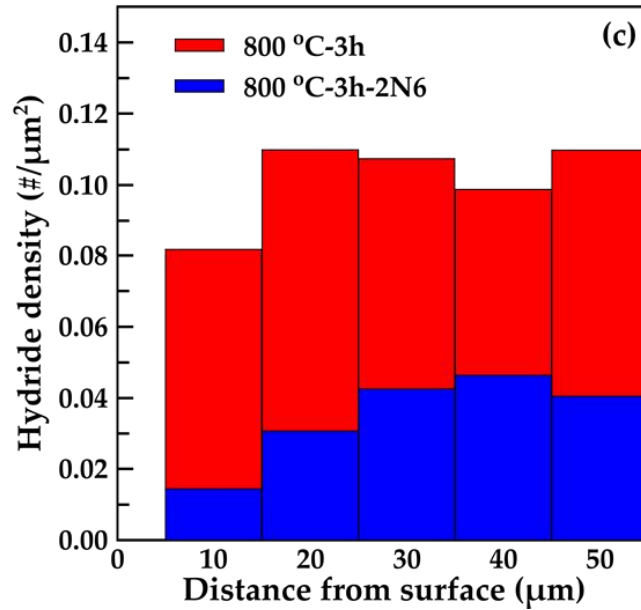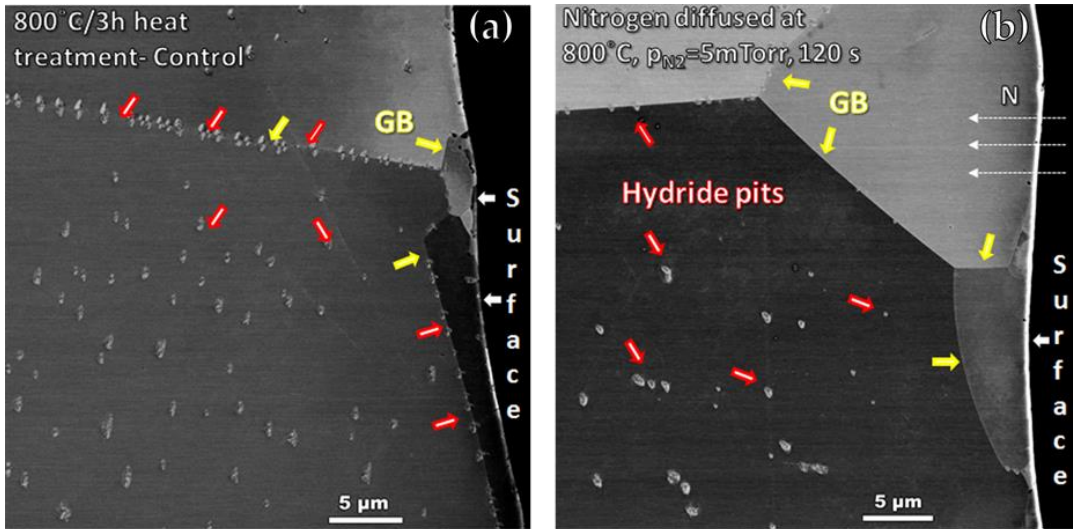
Figure 7: Microstructure of niobium coupon samples treated (a) without nitrogen atmosphere and (b) in nitrogen atmosphere show low hydride concentration for the nitrogen treated niobium surfaces. (c) The hydride density measured from the surface is nearly constant in the 800°C-3h (control) sample, and lower in the sample where surface N concentration is higher even up to distances of 50μm.

These observations provide the opportunity to seek a better mechanistic understanding of how nitrogen doping influences the kinetic stability of hydrogen and the

thermodynamic stability of hydride precipitates in niobium. Thus, the goal is to understand the mechanisms associated with interstitial nitrogen acting as a trapping site for hydrogen and how it inhibits hydride precipitation in niobium as observed in experiments. Therefore, first-principles calculations were used to examine the effect of nitrogen on hydrogen absorption and the stability of hydride precipitates in niobium.

3.2 Computational Details

First-principles calculations were performed using the Vienna Ab-initio Simulation Package (VASP) based on the density functional theory (DFT) (Georg Kresse and Hafner 1993; G. Kresse and Hafner 1994). The projector augmented wave (PAW) pseudopotentials (Blöchl, Jepsen, and Andersen 1994; Georg Kresse and Furthmüller 1996) using Perdew-Burke-Ernzerhof (PBE) (Blöchl 1994) exchange-correlation formulation were used to represent the nuclei and valence electrons of Nb, including six of the $4p$ electrons. A plane wave basis set with an energy cutoff of 550 eV, 350 eV and 550 eV were used for niobium, hydrogen and nitrogen atoms, respectively. The Monkhorst-Pack K-point mesh of 12 x 12 x 12 was employed to carry out the Brillouin-zone integrations (Monkhorst and Pack 1976) and the ions were relaxed with a force and energy convergence criteria of 0.01 eVÅ^{-1} and 10^{-6} eV respectively. The calculated niobium lattice parameter of 3.31 Å was found to be in good agreement with the reported experimental and theoretical values (Alefeld and Völkl 1978; Ford, Cooley, and Seidman 2013b).

3.3 Results

3.3.1 Suppression Effect of N Doping on Binding of H in Nb

Absorption of hydrogen and nitrogen is energetically favorable at interstitial tetrahedral (T) and octahedral (O) sites in niobium (-0.28 eV and -1.98 eV), respectively. A 2 x 2 x 2 body centered cubic niobium supercell (16 niobium atoms) was used to examine the binding behavior one hydrogen and one nitrogen atom within the niobium lattice, i.e. a concentration of 1/16. The binding energy (ΔE) for hydrogen at different interstitial sites in niobium with a nitrogen atom located at an octahedral site was calculated using the following equation:

$$\Delta E = E_{Nb_{16}N_1H_1} - (E_{Nb_{16}N_1} + 0.5 * E_{H_2}) \tag{1}$$

where $E_{Nb_{16}N_1H_1}$ represents the energy of the niobium lattice with nitrogen and hydrogen atoms present at their respective interstitial sites, $E_{Nb_{16}N_1}$ represents the energy of niobium lattice with a nitrogen atom doped at an octahedral site and E_{H_2} represents the energy of hydrogen in gas-phase. Negative values of the ΔE implies that hydrogen binding is energetically favorable, while positive values indicate that it is favorable for hydrogen to leave the interstitial site and go into another favorable site.

For the case of hydrogen doped at different tetrahedral sites near nitrogen, it was found that hydrogen binding was no longer energetically favorable at sites T1 and T2, identified in Figure 8. However, the binding energy gradually decreased and became negative for the interstitial sites located away from nitrogen, such as T3, T4 and O sites, as shown in Figure 8. Thus, nitrogen suppressed hydrogen binding in niobium, but the level of suppression gradually diminished for hydrogen present at interstitial sites farther

21

away from nitrogen, approximately 2.5 Å. Furthermore, the suppressing effect of nitrogen is dependent on the local concentration of both nitrogen and hydrogen present in niobium. Interestingly, both T4 and O interstitial sites away from nitrogen were found to have similar binding energies for hydrogen binding in niobium.
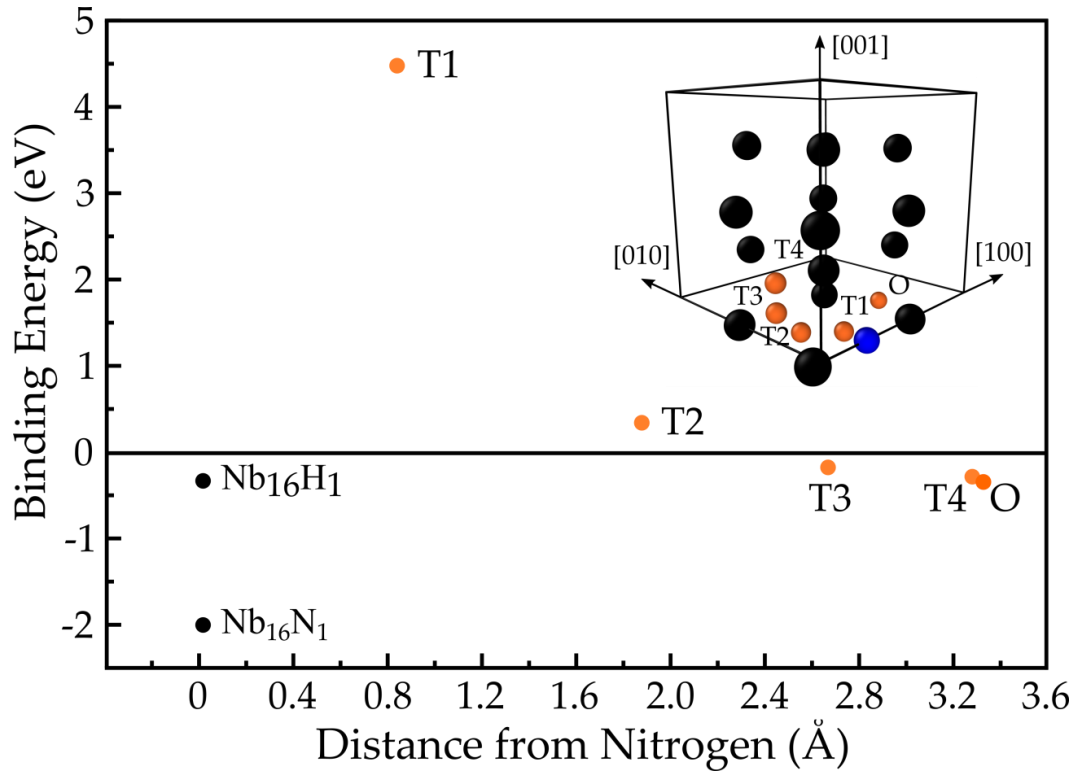
Figure 8: Plot of the binding energy of hydrogen at four different tetrahedral sites and one octahedral site near a nitrogen atom located at an octahedral site in niobium versus distance of interstitial sites away from the nitrogen atom. Niobium, hydrogen and nitrogen atoms are represented by dark grey, red and blue spheres, respectively.

To understand the effect of nitrogen on the binding energy of hydrogen in niobium, the electronic structure of bulk niobium with interstitially absorbed hydrogen and nitrogen atoms was examined using the electronic density of states (DOS) and valence

charge transfer calculations. This provides insights into the changes in bonding between the interstitial and the host metal atoms. The DOS curve describes the number of states available to be occupied per interval of energy at each energy level (Pronsato, Pistonesi, and Juan 2004). To calculate the valence charge transfer resulting from the addition of different interstitial atoms, the ground state non-interacting valence charge densities were subtracted from the valence charge density of the interacting system (P. Garg, Adlakha, and Solanki 2018; P. Garg et al. 2017). Thus, the valence charge transfer ($\Delta\rho$) was calculated as:

$$\Delta\rho = \rho_{Nb-H-N} - \rho_{Nb} - \rho_{H} - \rho_{N} \qquad (2)$$

where ρ_{Nb-H-N} represents the valence charge density of interacting Nb-H-N system, and ρ_{Nb}, ρ_{H} and ρ_{N} represent the valence charge density of non-interacting and isolated niobium, hydrogen and nitrogen atoms, respectively. The VESTA (visualization for electronic and structural analysis) software package (Momma and Izumi 2008) was used to extract and visualize the valence charge transfer contours from the first-principles calculations.

First, the DOS curve of bulk niobium with interstitially absorbed hydrogen was examined, i.e., without nitrogen atoms. The DOS curve shows an overlap between the states of niobium and hydrogen at -7 eV indicating the formation of covalent bonds between niobium and hydrogen atoms see figure A1a in appendix. A similar overlap characteristic of covalent bonding has been reported in previous studies for various metal hydride systems (Aboud and Wilcox 2010; Gupta 1982; Pulkit Garg et al. 2018). The covalent bonding was further verified by assessing the valence charge density around

23

niobium and hydrogen atoms shown in figure A1b in appendix. Here, the valence charge
around black niobium atoms was attracted towards the orange hydrogen atom (from the
cyan toward the yellow iso-charge surface), contributing to the energetic preference of
forming a covalent bond. However, in the presence of nitrogen at an O site (blue atom
that appears gray) and hydrogen at the T1 tetrahedral site, the states of nitrogen
overlapped with the states of niobium and hydrogen (Figure 9a). As a result, the
interactions between the states of niobium and hydrogen were interrupted by the presence
of nitrogen, suggesting a decrease in the extent of covalent bonding between niobium and
hydrogen atoms. Also, the development of repulsive interactions due to the accumulation
of valence charge between hydrogen and nitrogen atoms (yellow iso-charge surface,
Figure 9b) made the structure energetically unstable. This indicates a positive energy for
hydrogen binding at the T1 site in bulk niobium with a nitrogen atom at an O site. Similar
effects of nitrogen on covalent bonding between niobium and hydrogen were observed
when hydrogen was present at the T2 tetrahedral site (Figure 9c). However, the repulsive
interactions between nitrogen and hydrogen are weaker, indicated smaller binding
energy, due to the increased distance between them at the T2 site (Figure 9d). When a
hydrogen atom is located at a T4 or O site, states of niobium and hydrogen overlapped
(Figure 9e), irrespective of the presence of nitrogen in bulk niobium. Thus, the
interactions between niobium and hydrogen were not affected by nitrogen and the
covalent bonding between niobium and hydrogen atoms was conserved when hydrogen
atom was present away from nitrogen. Furthermore, the valence charge accumulated
around the hydrogen and the nitrogen atom was attracted towards the charge depleted

region (cyan iso-surface, Figure 9f-g) between them, contributing to the energetic preference of hydrogen to occupy T4 or O site in niobium.

(a)

(b)

(c)

(d)

(e)

(f)

(g)
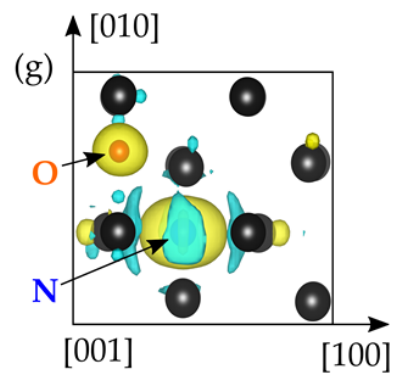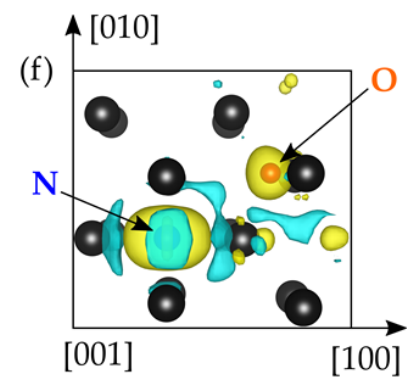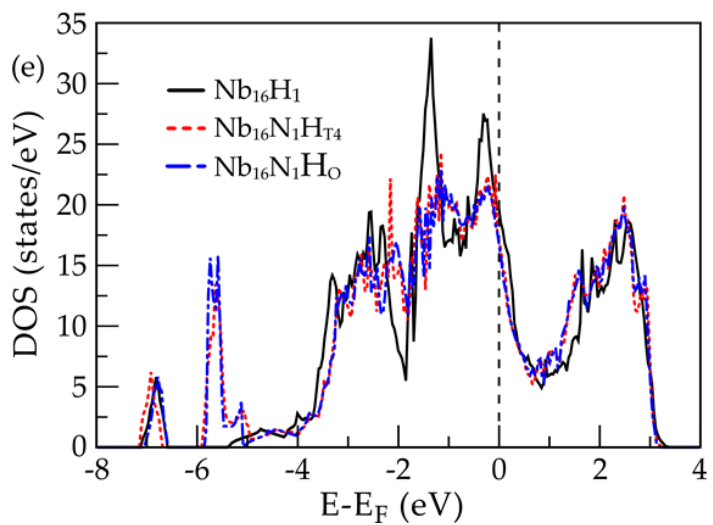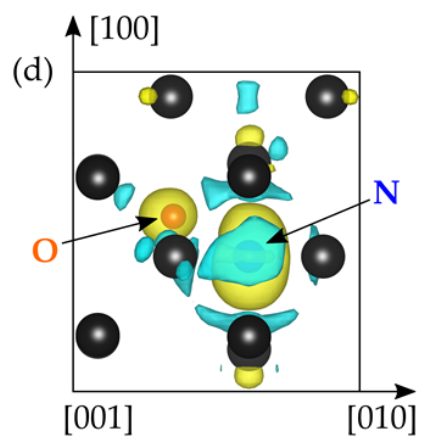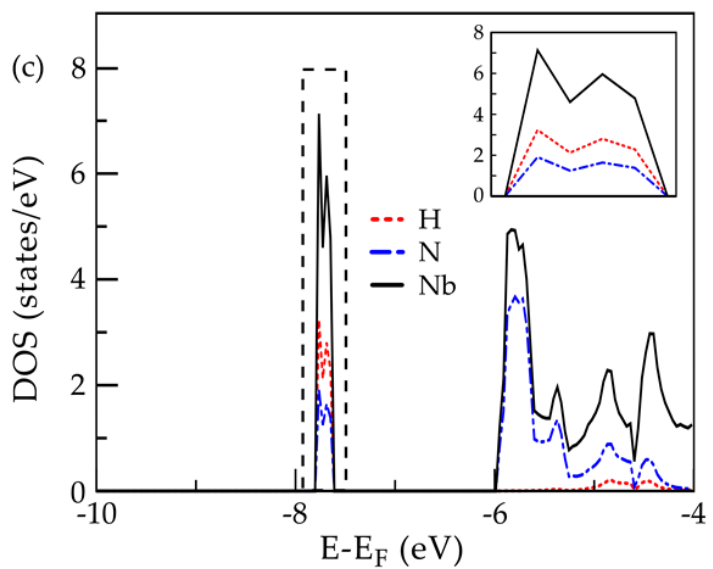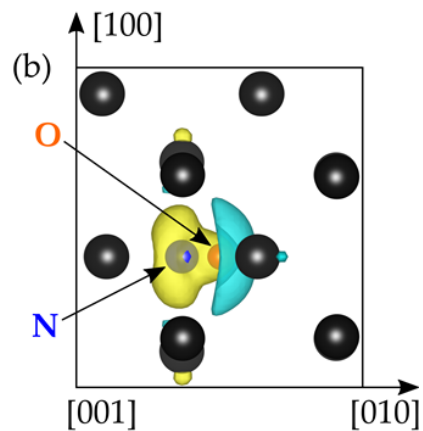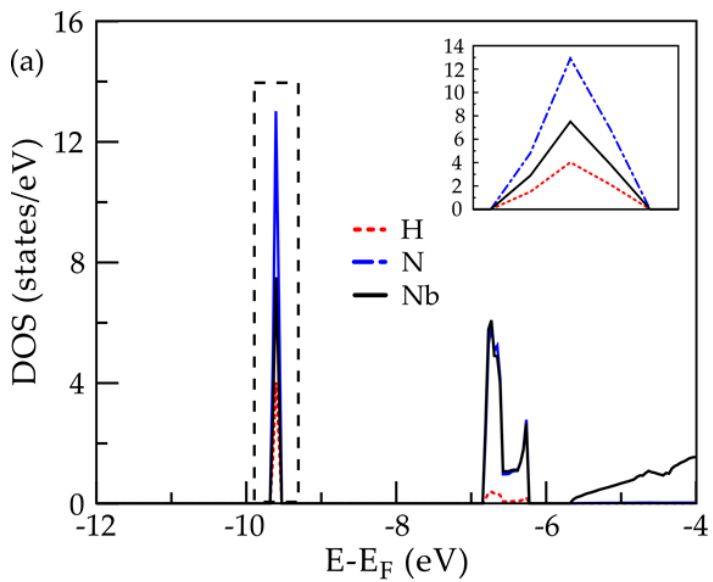
Figure 9: (a) DOS and (b) charge transfer of $Nb_{16}N_1$ with an H atom at the T1 site. (c) DOS and (d) charge transfer of $Nb_{16}N_1$ with H atom at T2 site. (e) DOS for $Nb_{16}H_1$ compared to the DOS of $Nb_{16}N_1$ with one H atom at the T4 site and for one H atom on the O site. (f, g) The valence charge transfer plots for $Nb_{16}N_1$ with H atom at T4 site and O sites, respectively. Yellow and cyan iso-charge surfaces represent $0.027e/Å^3$ of charge accumulation and depletion, respectively in (b), (d), (f) and (g). Niobium atoms are represented by black spheres in the valence charge transfer contours.

3.3.2 Effect of N on H Diffusion in Nb

Next, the effect of nitrogen on the kinetic stability of hydrogen in the niobium lattice was investigated. It is critical to study the effect of nitrogen on the activation energy barrier for hydrogen diffusion as it affects the migration and retention of hydrogen in bulk niobium. To determine the activation barriers and the minimum energy pathways associated with hydrogen diffusion, the nudged elastic band (NEB) method (Henkelman and Jónsson 2000) was used within the DFT framework. The NEB calculations were performed using the fast-inertial relaxation engine (FIRE) optimizer (Bitzek et al. 2006) with eight intermediate images, selected after reaching convergence based on the number of images. Other input parameters and convergence criteria were kept the same as for the ground state calculations. In the niobium lattice, the activation energy barrier for hydrogen diffusion from one tetrahedral site to the nearest tetrahedral site was found to be 0.18 eV (Figure 10a), which compares well with the reported literature value (Lu et al. 2012). However, with the addition of nitrogen, the activation energy barrier along the minimum energy path for hydrogen diffusion in the niobium lattice increased significantly as shown in figure 10b. In the presence of nitrogen in niobium, a hydrogen

27

atom will diffuse from one tetrahedral site to the 2nd nearest tetrahedral site, not the nearest tetrahedral site, via a metastable octahedral site with an activation energy barrier of 0.457 eV. Thus, nitrogen increases the energy barrier for hydrogen diffusion and hence, decreases the rate of hydrogen diffusion in bulk niobium.
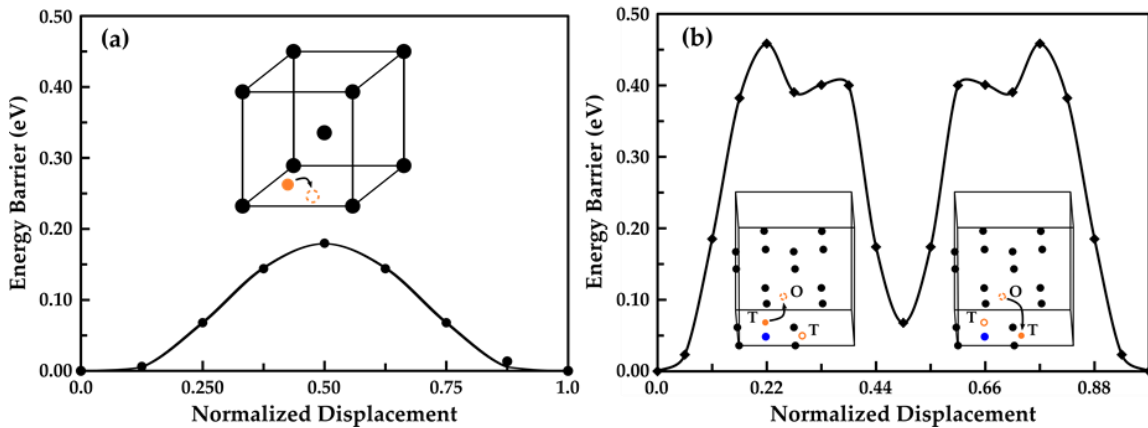
Figure 10: Activation energy barrier for hydrogen diffusion from one tetrahedral site to another (a) in bulk niobium and (b) in niobium near a doped nitrogen atom. Niobium, hydrogen and nitrogen atoms are represented by black, orange and blue spheres, respectively.

3.3.3 Effect of N Doping on Hydride Stability in Nb

In addition to the thermodynamic and kinetic stability of hydrogen, nitrogen also affects the stability of hydride precipitates in niobium. Therefore, studying the effect of nitrogen on the stability of beta niobium hydride ($\beta - NbH$) precipitates and why the low hydride concentration in nitrogen treated cavity surfaces will provide understanding that can lead to increased niobium cavity performance. To accomplish this, a $\beta - NbH$ unit cell (Figure 11a) was introduced in 3 x 3 x 3 periodic replication of the niobium unit cell rotated along [110] and [1$\bar{1}$0] direction (108 atoms) (Figure 11b). Next, the niobium

matrix embedded with a $\beta - NbH$ precipitate was energetically relaxed to obtain an equilibrium structure followed by introducing nitrogen at different interstitial sites in niobium. The formation energy (ΔE) of nitrogen at different interstitial sites in niobium embedded with a $\beta - NbH$ precipitate was calculated according to the following equation:

$$\Delta E = E_{near} - E_{away} \tag{3}$$

where E_{near} and E_{away} represent the total energy of the niobium matrix embedded with $\beta - NbH$ precipitate and doped with a nitrogen atom at different octahedral sites near and away from the hydrogen atoms, respectively. Thus, a positive value of ΔE represents a decrease in the energetic stability of hydride precipitates in the niobium matrix when doped with nitrogen atom. The positive formation energies in Table 1 suggest that nitrogen decreased the stability of $\beta - NbH$ precipitate in the niobium matrix (Table 1).

Table 1: The formation energy of niobium matrix embedded with $\beta - NbH$ precipitate and doped with nitrogen atom at different interstitial sites with respect to the nitrogen atom doped far away from the hydrogen atoms.

Position of N	ΔE (eV)
Octa 1	0.93
Octa 2	0.78
Octa 3	1.45
Octa 4	1.19

The decrease in the stability of $\beta - NbH$ with the presence of nitrogen in niobium can be understood through the electronic DOS and valence charge transfer calculations. As discussed earlier, the overlap between the states of niobium and hydrogen corresponds to the covalent bonding between niobium and hydrogen atoms. Here, the overlap corresponds to the covalent bonding in $\beta - NbH$ precipitate (Figure 11c). However, the -7 eV peak disappeared upon addition of nitrogen indicating that the states of hydrogen no longer overlap with the states of niobium (Figure 11d). Hence, the covalent bonding between niobium and hydrogen atoms was disrupted by nitrogen. Valence charge transfer calculations further explain the instability of the hydride precipitate in the presence of nitrogen in the niobium matrix. In the absence of nitrogen, charge depleted (cyan iso-surface) from the niobium atoms in the hydride precipitate was accumulated (yellow iso-surface) around the hydrogen atoms (Figure 11e). However, in the presence of nitrogen, the valence charge from niobium atoms in the precipitate and the matrix is now attracted towards nitrogen due to its partially anionic nature in niobium (Figure 11f). As a result, the niobium hydrogen covalent bonding in hydride precipitate became weaker in the presence of nitrogen, leading to a decrease in the energetic stability of $\beta - NbH$ precipitates in the niobium matrix.
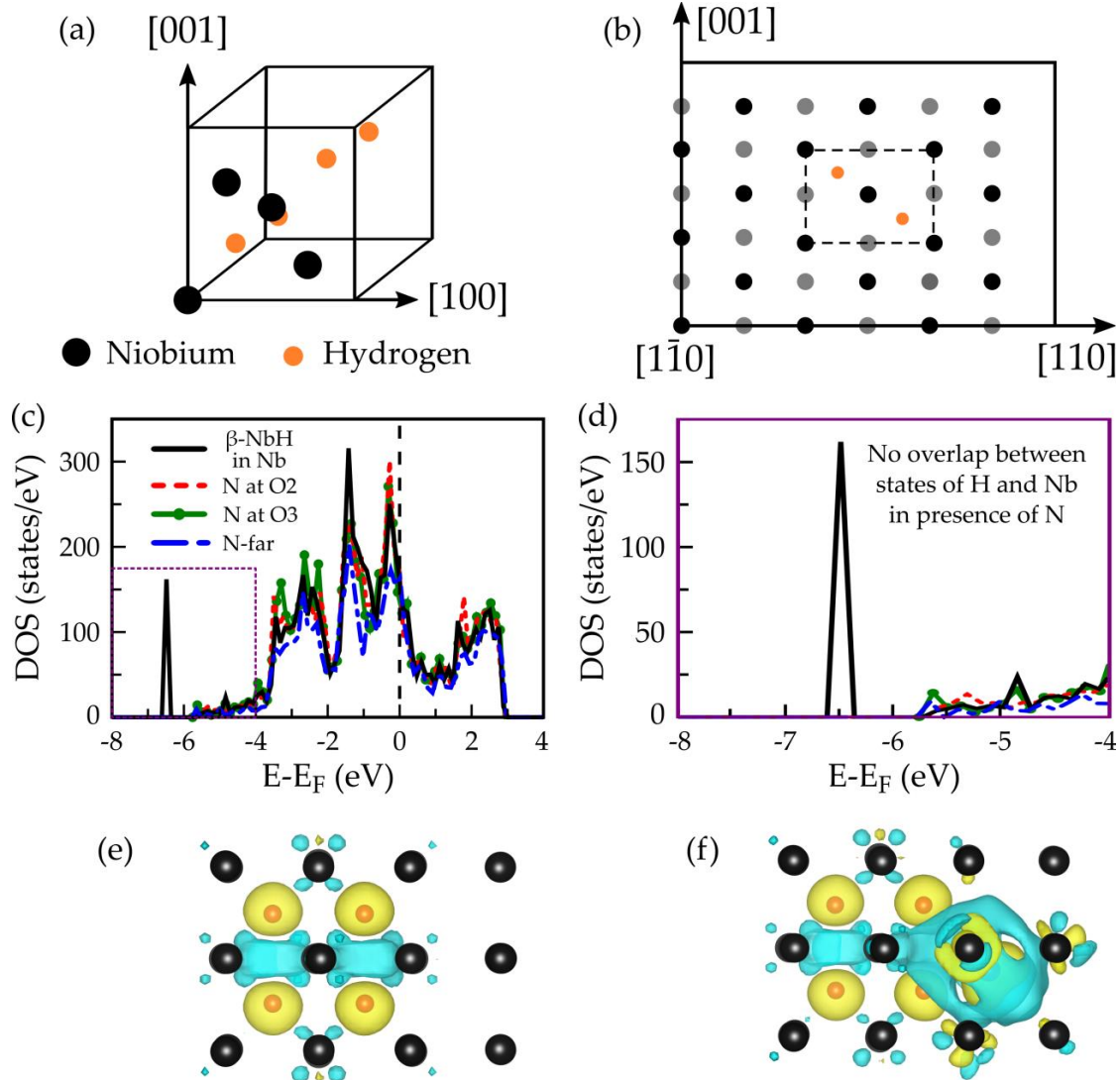
Figure 11: Schematic of a) $\beta-$NbH unit cell with face centered orthorhombic structure and b) a $\beta-$NbH unit cell embedded in the niobium matrix. Black and grey spheres represent niobium atoms on two different planes. c) Density of states for the niobium matrix embedded with $\beta-$NbH and doped with nitrogen atoms at different octahedral (O2, O3 and far away) sites. d) Zoomed in DOS curves showing the absence of hydride peak upon addition of nitrogen in niobium. Valence charge transfer contours for e) niobium with $\beta-$NbH and f) niobium with $\beta-$NbH and doped with nitrogen at the far away octahedral site. Yellow and cyan iso-charge surfaces respectively represent $0.027e/Å^3$ of charge accumulation and depletion. Niobium atoms are represented by dark

grey spheres, hydrogen atoms are represented by orange spheres and nitrogen atom is represented by a blue sphere (below the iso-surface) in 11e and 11f.

3.4 Conclusions

In conclusion, these first-principles calculations enable identification of the mechanisms and driving forces associated with the observed low hydride concentration near the nitrogen treated niobium coupon surfaces. Nitrogen doping significantly affects the kinetic stability of hydrogen and the thermodynamic stability of hydride precipitates in niobium. In the presence of nitrogen, hydrogen binding in niobium is suppressed but the suppressing effect was dominant only in the proximity of nitrogen, approximately up to 2.5 Å away. Furthermore, the suppressing effect of nitrogen on hydrogen binding in niobium was due to the weakening of covalent bonds between the niobium and hydrogen atom, understood through electronic DOS and valence charge transfer calculations. Nitrogen also altered the minimum energy path for hydrogen diffusion from one tetrahedral site to another, leading to a notable increase in the activation energy barrier for hydrogen diffusion in the niobium lattice. Furthermore, the $\beta - \mathrm{NbH}$ precipitate became energetically unstable near a nitrogen atom in the niobium matrix since the niobium hydrogen covalent bonding is disrupted by nitrogen. Thus, introduction of nitrogen into the surface of niobium cavities significantly decreased the thermodynamic and kinetic stability of hydrogen in niobium and consequently reduced the likelihood of hydride precipitation, which were demonstrated experimentally using simple metallographic techniques. The hydride suppression due to the presence of nitrogen could be one of the contributing reasons for the increased quality factors beyond the traditional

SRF Nb recipes in cavities using this nitrogen doping recipe that are currently being produced for the LCLS-II upgrade (A Grassellino and A Romanenko and D Sergatskov and O Melnychuk and Y Trenikhina and A Crawford and A Rowe and M Wong and T Khabiboulline and F Barkov 2013; Pashupati Dhakal et al. 2015). However, increase in quality factors in nitrogen-doped cavities has also revealed an issue of flux trapping due to the presence of defects in bulk Nb. Further studies to understand the effect of nitrogen on the residual surface resistance and the magnetic flux trapping in niobium will help determine the overall effectiveness of nitrogen in improving the performance of niobium for SRF applications.

CHAPTER 4

4 HYDROGEN SEGREGATION AT DISLOCATION CORE STRUCTURES AND

GRAIN BOUNDARIES IN NIOBIUM

4.1 Introduction

The low temperature plasticity in body centered cubic (BCC) metals, such as niobium

is predominately controlled by the screw dislocation core structure and its motion, which

leads to increase in the yield stress with decreasing temperature as well as non-Schmid

behavior (Ventelon et al. 2013; Christian 1983; Caillard and Martins 2003; Argon 2008).

First-principles studies have been employed to study such dislocation core structure and

its properties including lattice resistance to the motion of screw dislocations (Gröger and

Vitek 2012; Vitek † 2004; L. Dezerald et al. 2014; Rodney et al. 2017). Through ab initio

calculations, it has been argued that the strain rate sensitivity and breakdown of Schmid

behavior can be attributed to the non-planar nature of the $1/2\langle 111 \rangle$ screw dislocation

core (Duesbery, Vitek, and Bowen 1973; Duesbery and Vitek 1998; Ito and Vitek 2001;

Itakura, Kaburaki, and Yamaguchi 2012a), and the existence of two possible equilibrium

core structures (V. Vitek and Paidar 2008) both having D3 symmetry along the <111>

zone (Gordon, Neeraj, and Mendelev 2011; Itakura, Kaburaki, and Yamaguchi 2012a;

Ramasubramaniam, Itakura, and Carter 2009). Furthermore, the existence of a metastable

split-core configuration during dislocation glide across the lattice creates a tendency for

partial kink nucleation (Itakura, Kaburaki, and Yamaguchi 2012a; Ventelon et al. 2013;

Weinberger, Tucker, and Foiles 2013).

In general, due to non-planar nature of the dislocation core, the plastic deformation of BCC metals is observed to be significantly different than other close-packed metals (Christian 1983). The plastic behavior of BCC metals is further complicated with addition of impurities like hydrogen (H) in Nb, since the addition of impurities can affect the slip by modifying dislocation core structure. For instance, the presence of solutes/impurities can significantly modify the elastic, chemical and electronic interactions between the dislocations (Cottrell 1948; Hirth and Lothe 1966; Bhatia, Groh, and Solanki 2014), thereby increasing the yield strength of material. Furthermore, pure Nb is a principal material for manufacturing superconducting radio frequency (SRF) cavities, but it readily absorbs hydrogen during fabrication and subsequently leads to hydride precipitation in Nb when cooled to cryogenic temperatures (Hardie and McIntyre 1973; Tao et al. 2013; Pulkit Garg et al. 2018). Presence of such defects (interstitial H and hydrides) not only alters the plastic deformation behavior of Nb, but also degrades its superconducting properties (Knobloch 2003; Trenikhina et al. 2015; P. Garg et al. 2018).

Additionally, grain boundaries act as preferential sites for impurity segregation (Solanki et al. 2013; Sadananda and Vasudevan 2011). Aggregation of sufficient concentration at the interface can lead to intergranular failure (Rice and Wang 1989). High diffusivity of the hydrogen atoms allows them to permeate the microstructure rapidly along the GB networks, dislocations and voids etc. leading to mechanical degradation (Solanki et al. 2013; Rajagopalan, Tschopp, and Solanki 2014). The local atomic structure is known to significantly affect the solute segregation behavior (I. Adlakha, Tschopp, and Solanki 2014; Ilaksh Adlakha 2015). The GB character often

35

encompasses five degrees of freedom associated with the misorientation between the crystallographic orientations of the two adjoining grains. Two degrees of freedom are associated with the GB plane while three degrees of freedom are used to define the misorientation between the two grains. The microscopic degrees of freedom cover the local structure arrangement that is dependent on the translations between adjoining grains which is important as well as the localized dislocation structure of the boundary. Experimental studies are often limited in examining solute segregation near GBs because of the complicated atomic structure. On the other hand, atomistic and first principle calculations can be effectively utilized to explore the complicated interactions between the GB structure and solute atoms (Yamaguchi, Shiga, and Kaburaki 2004; Yamaguchi et al. 2011). Therefore, this work utilizes *ab initio* methods to investigate the effect of interstitial hydrogen on $1/2\langle 111 \rangle$ screw dislocation core and $\Sigma 5$ symmetric tilt grain boundaries (STGBs) in Nb and elucidate the effect of impurity on plastic deformation in Nb. Additionally, electronic structure calculations through density of states and valence charge transfer were also performed along with equilibrium dislocation core structure characterization to underpin the effect of hydrogen on the dislocation core properties.

4.2 Computational Details

4.2.1 Screw Dislocation Core Structure

The *ab initio* simulation cell for screw dislocation core structure was constructed with a quadrupolar arrangement of screw dislocation dipoles using Stroh's anisotropic field and elastic constants of Nb (Stroh 1958; Clouet, Ventelon, and Willaime 2009). To

accommodate the plastic strain induced by dislocation dipole and to minimize the elastic energy of simulation cell, the supercell vectors $(\vec{c}_1, \vec{c}_2, \vec{c}_3)$ were selected as:

$$\vec{c}_1 = n\vec{a}_1 - q\vec{a}_3, \vec{c}_2 = \frac{n}{2}\vec{a}_1 + m\vec{a}_2 + (\frac{1}{2} - \frac{q}{2})\vec{a}_3, \vec{c}_3 = \vec{a}_3 \qquad (4)$$

where $\vec{a}_1 = 1/3\ [\bar{1}\bar{1}2]$, $\vec{a}_2 = 1/2\ [1\bar{1}0]$, $\vec{a}_3 = 1/2\ [111]$, $(n,m) = (15,9)$ for 135 atom supercell and $q = -1/_3 m$ (L. Dezerald et al. 2014). The *ab initio* calculations were performed using density functional theory (DFT) based Vienna Ab-initio Simulation Package (VASP) (Georg Kresse and Hafner 1993; G. Kresse and Hafner 1994). The simulation cell was relaxed using VASP to obtain equilibrium dislocation core structures. Hydrogen atoms were then added to both the equilibrated dislocation core structures at the interstitial tetrahedral site, stable interstitial position in perfect lattice (P. Garg et al. 2018; Ford, Cooley, and Seidman 2013a), followed by atomic relaxations. Spin-polarized calculations were performed to relax the dislocation dipole structure with and without hydrogen with cut-off energy of 550 eV, energy convergence of 10^{-5} eV and 0.01 eVÅ^{-1} of force tolerance. The atom positions were relaxed at their atomic positions while maintaining a constant volume with a k point mesh of $1 \times 1 \times 16$ to minimize the energy of the dislocation dipole. The changes in electronic structure of dislocation core due to the presence of interstitial hydrogen were examined through electronic density of states and valence charge transfer calculations.

4.2.2 Symmetric Tilt Grain Boundaries

The equilibrium grain boundary (GB) structures were modeled using empirical interatomic potentials molecular dynamics (MD) simulations. The $\Sigma 5(210)$ and $\Sigma 5(310)$

symmetric tilt grain boundary (STGB) system was created in Large-scale

Atomic/Molecular Massively Parallel Simulator (LAMMPS)(Plimpton 1995) with semi-

empirical embedded atom method (EAM) potential for niobium(Fellinger, Park, and

Wilkins 2010). The equilibrium grain boundary structures were determined using a bi-

crystal simulation cell with 3D periodic boundary conditions and sufficiently large grains

in the perpendicular direction to obtain minimum energy GB structures (Rittner and

Seidman 1996; Rajagopalan et al. 2017; I. Adlakha et al. 2014). For instance, the $\Sigma5(210)$

grain boundary was modeled by two (210) oriented slabs of Nb each, reflected with

respect to the x-z plane followed by an atom deletion technique and energy minimization

using a nonlinear conjugate gradient method (see Figure 1b)(Rajagopalan et al. 2014;

Solanki et al. 2013; Tschopp et al. 2012). All atoms of the GB supercells were allowed to

relax to an energy convergence of $<10^{-6}$ eV(Wachowicz and Kiejna 2008; I. Adlakha,

Garg, and Solanki 2019). Next, due to the size constraints of first-principles methods

smaller supercells with one periodic length along the GB and few atomic planes (20-30

atomic planes) perpendicular to the GB plane were obtained from the bi-crystal

simulation cell of MD calculations. The smaller supercells for different grain boundaries

with negligible grain boundary interactions across the periodic images were relaxed

within DFT framework. The *k* point mesh for each of the GB supercells was selected,

after extensive *k* point sampling, based on the convergence studies (see table A1 in

appendix) and the atoms were relaxed with 10^{-6} eV energy tolerance while maintaining a

constant volume and shape of the supercells.

4.3 Results

4.3.1 Hydrogen Segregation at Screw Dislocation Core Structure

The displacement field around the relaxed Nb dislocation core is shown (Fig. 12a) using the differential displacement (DD) map (V Vitek, Perrin, and Bowen 1970; Vo Vitek 1974) and the dislocation core energy is 0.2 meV/b, where b is the Burgers vector, on (111) plane in bcc Nb. The Nb atoms in three different colors are projected on the (111) plane and belong to three different layers before the dislocation was introduced. The relative displacement of an atom in the $1/2 \langle 111 \rangle$ direction relative to its nearest neighbor is represented by an arrow pointing between the atoms as compared to the perfect crystal. The length of the arrow is proportional to the magnitude of relative displacement between the atoms. A closed triplet of arrows around a dislocation gives a Burger's vector displacement. Thus, the $1/2 \langle 111 \rangle$ screw dislocation core in Nb has a non-degenerate (or symmetric or easy core) configuration, also observed in previous works (Frederiksen and Jacobsen 2003; Itakura, Kaburaki, and Yamaguchi 2012b; Domain and Monnet 2005). Next, a hydrogen atom was introduced at the most stable interstitial site, determined from the work of (Zhao and Lu 2011), at each of the equilibrium screw dislocation cores Fig. 12b). The displacement field in the DD map shows the transformation of the dislocation core from a non-degenerate to degenerate (hard core) dislocation core with the addition of H atom. Local environment around the solute atom like the number of neighbors and atomic distances, and the nucleation of second phase precipitates can be attributed to the stability of hard core configuration.

39

Similar stabilization of the hard core configuration has been observed with the addition of carbon in BCC iron (Ventelon et al. 2015).
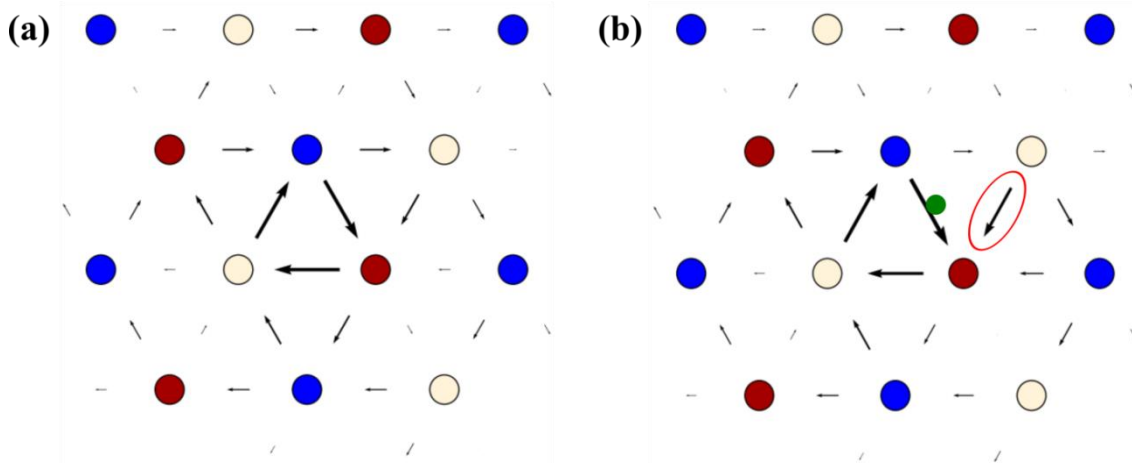
Figure 12: Differential displacement map of (a) the non-degenerate dislocation core in Nb and (b) the degenerate dislocation core in Nb with H. The blue, maroon and yellow circles represent Nb atoms at different (111) planes, while the H atom is represented by the green circle.

To further understand the H atom and screw dislocation interaction, the electronic structure of screw dislocation core with interstitial hydrogen was examined using the electronic density of states (DOS) and valence charge transfer calculations. This provides insights into the changes in bonding between the interstitial and the dislocation core atoms (P. Garg et al. 2017). The DOS curve describes the number of states available to be occupied per interval of energy at each energy level (P. Garg, Adlakha, and Solanki 2018). Valence charge transfer due to the addition of hydrogen was calculated by subtracting the ground state non-interacting valence charge densities of dislocation core and hydrogen from the valence charge density of the interacting hydrogen dislocation

core system (P. Garg, Bhatia, and Solanki 2019; P. Garg, Adlakha, and Solanki 2019).

Charge density contours from the first-principles calculations were obtained using

VESTA (visualization for electronic and structural analysis) software package (Momma

and Izumi 2008).
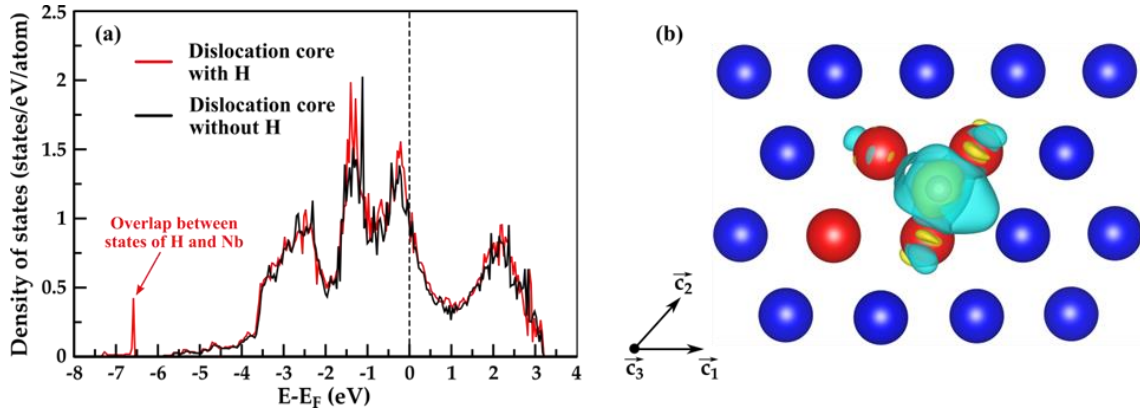
Figure 13: (a) The effect of hydrogen addition near the screw dislocation on the electronic density of states in Nb with and without hydrogen atom. (b) Valence charge density transfer at the dislocation core structure between the Nb atoms and hydrogen atom. Charge is depleted from Nb atoms and accumulated around hydrogen. Yellow and cyan iso-charge surfaces represent 0.01 $e\mathring{A}^{-3}$ of charge accumulation and depletion, respectively. The atoms are colored according to common neighbor analysis such that dislocation core atoms are red and bcc atoms are blue.

Figure 13a shows the DOS curves for screw dislocation core in niobium with and

without interstitial hydrogen. The DOS curve below Fermi level (0 eV) corresponds to

the occupied bonding states; whereas, the curve above Fermi level represents the

unoccupied antibonding states. The DOS curve of screw dislocation core was found to

match the DOS curve reported in literature (L. Dezerald et al. 2014). An additional peak

at -6.5 eV was observed in the DOS curve of screw dislocation core with interstitial

hydrogen due to the overlap of *1s* states of hydrogen with states of niobium. Thus, the additional peak indicates to presence of covalent bonding between hydrogen and niobium and therefore represents the possibility of nucleation of niobium hydride precipitate at the screw dislocation core (P. Garg et al. 2018). The valence charge transfer calculation further assesses the covalent bonding between hydrogen and niobium atoms at the dislocation core. The valence charge of dislocation core niobium atoms (red spheres) is depleted and gets accumulated around the hydrogen atom (small orange atom below iso-charge surface) promoting the formation of covalent bond between hydrogen and niobium (figure 13b). Thus, valence charge transfer calculation also supports hydride precipitation as a contributing factor to the stability of hard core configuration upon presence of hydrogen at screw dislocation core. Valence charge transfer contours are plotted at an iso-charge surface value of $0.01\ e\text{Å}^{-3}$, where yellow and cyan iso-charge surfaces respectively represent charge accumulation and depletion. Niobium atoms at the dislocation core are represented by red spheres while the blue spheres represent bulk niobium atoms.

To understand the changes in plasticity of niobium in presence of hydrogen, the effect of hydrogen atoms on the mobility of screw dislocations in Nb was determined using first-principles methods. To determine the associated energy barriers and the minimum energy pathways, the NEB method with FIRE optimizer and eight intermediate images was used within the DFT framework. Other input parameters and convergence criteria were kept the same as for the ground state calculations.
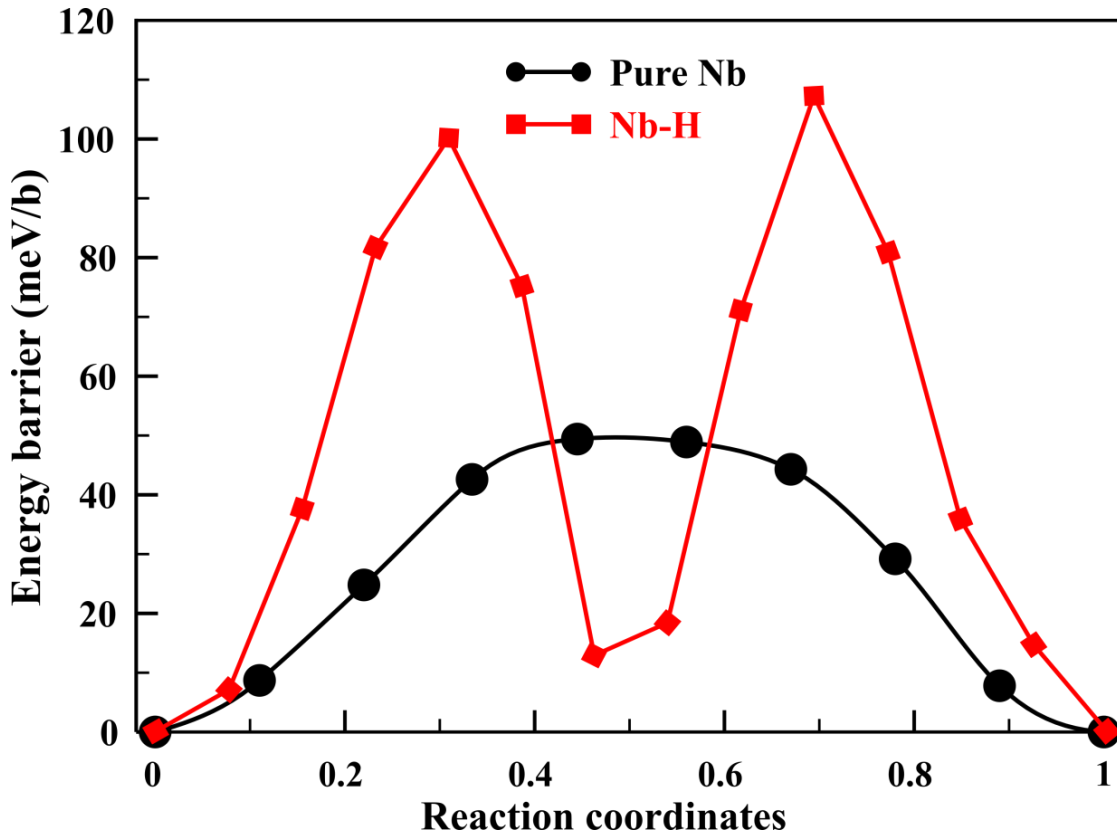
Figure 14: Peierls energy barrier for a screw dislocation dipole in niobium with and without hydrogen atom at the dislocation cores. The minimum energy paths were determined using NEB method within the DFT framework.

First, the Peierls energy barrier for glide of screw dislocation on (111) plane of pure Nb was determined by constrained minimization of the screw dislocation dipole. Both the dislocations were displaced in the same direction by one Peierls distance between the initial and final states, so that the distance between the two dislocations remains constant. The predicted Peierls energy barrier curve has a single hump and appears sinusoidal (figure 14). The energy barrier for gliding of $1/2 \langle 111 \rangle$ screw dislocation in Nb was found to be ~50meV/b, which is in good agreement with the values reported in literature (Lucile Dezerald et al. 2016; L. Dezerald et al. 2014). Next, the constrained minimization

of the screw dislocation cores with hydrogen atoms in the vicinity was performed to determine the effect hydrogen on dislocation motion. The NEB calculations were performed with twelve intermediate images selected after convergence studies based on the number of images. The presence of hydrogen significantly affected the energy barrier for dislocation motion as shown in figure 14. In the presence of hydrogen, the energy barrier increased to ~100meV/b with a saddle point representing the metastable state between the two unstable configurations. The increase in energy barrier for glide of screw dislocations upon addition of hydrogen is due to the transformation of dislocation core to a hard core configuration in the presence of hydrogen. The stability of non-planar dislocation core stems from the development of attractive bonding between hydrogen and niobium. Thus, presence of hydrogen significantly alters the plastic behavior of niobium by increasing the stability of non-planar dislocation core thereby increasing the energy barrier for dislocation motion leading to solute hardening.

4.3.2 Hydrogen Segregation at $\Sigma 5$ STGBs

The equilibrium grain boundary structures were obtained after first-principles relaxation for $\Sigma 5(210)$ and $\Sigma 5(310)$ STGBs with atoms colored according to atomic volume variation in the simulation cell. Figure 15a shows significant variation in the atomic volume along the grain boundary plane (represented by black dash line) in $\Sigma 5(210)$ GB highlighting different potential sites for hydrogen segregation. A hydrogen atom was placed at each of the atomic sites (P) around the grain boundary plane and the computational cell was relaxed using the conjugate gradient energy minimization process

in VASP. The potential energy of the simulation cell was calculated and the process was

repeated for each of the interstitial sites across Σ5(210) and Σ5(310) STGBs (figure 15).
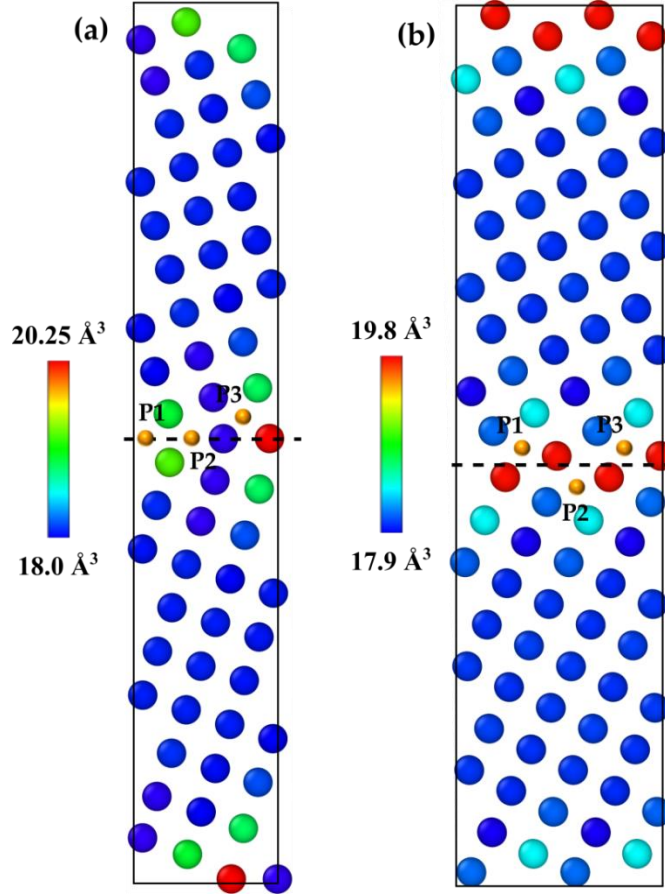
Figure 15: Different interstitial sites available for H atom segregation at (a) Σ5(210) GB
and (b) Σ5(310) GB. Niobium atoms are colored according to the atomic volume without
hydrogen estimated by Voronoi tessellation.

The segregation energy of hydrogen atom at an interstitial site (E_{seg}^P) was calculated

using:

$$E_{seg}^P = E_{GB}^P - E_{GB} - (E_{bulk}^H - E_{bulk}) \tag{5}$$

where, E_{GB}^{P} and E_{GB} are the potential energies of the GB structure with and without

hydrogen atom at the interstitial site P. E_{bulk}^{H} and E_{bulk} are the potential energies of a

single crystal Nb with and without interstitial hydrogen atom. Table 2 shows the

calculated segregation energy of hydrogen atom at different interstitial sites around

Σ5(210) and Σ5(310) STGBs. A negative value of segregation energy represents that the

particular interstitial site is energetically favorable for H segregation. In case of Σ5(210)

GB, interstitial site P1 has the most negative value of segregation energy (-0.09 eV) and

therefore the most stable for H segregation along the grain boundary plane. Similarly, in

Σ5(310) GB interstitial site P1 is the most stable with segregation energy of -0.02 eV.

Table 2: Hydrogen segregation energy (E_{GB}^{P}, eV) at different interstitial sites around
Σ5(210) and Σ5(310) STGBs.

Hydrogen segregation energy (eV)		
Position of H	Σ5(210)	Σ5(310)
P1	-0.09	-0.02
P2	0.05	0.04
P3	0.03	0.04

4.3.3 Effect of Nitrogen on Hydrogen Segregation at Σ5 STGBs

First, the segregation energy of nitrogen at the interstitial sites around the grain

boundaries without any hydrogen was calculated to determine the effect of nitrogen on

segregation behavior of hydrogen at Σ5 STGBs. A nitrogen atom was added each of the

46

interstitial sites (P) at Σ5(210) and Σ5(310) GBs and the segregation energy was calculated using equation 5. In case of Σ5(210) GB, P3 is the most favorable site for N segregation with segregation energy of -0.42 eV, whereas P1 is the energetically most favorable site for N segregation at Σ5(310) GB (Table 3).

Table 3: Segregation energy (E_{GB}^{P}, eV) of nitrogen at different interstitial sites around Σ5(210) and Σ5(310) STGBs.

Nitrogen segregation energy (eV)		
Position of N	Σ5(210)	Σ5(310)
P1	-0.11	-0.38
P2	-0.08	-0.36
P3	-0.42	-0.35

Next, the effect of nitrogen on the segregation energetics of hydrogen at Σ5(210) and Σ5(310) GBs in niobium was investigated within the first-principles framework. First, the hydrogen atom was added at the most stable interstitial site followed by nitrogen atom at its most stable interstitial site at each of the grain boundaries. The co-segregation energy (E_{co-seg}) of hydrogen and nitrogen at the grain boundary was calculated using the following equation:

$$E_{co-seg} = E_{GB-H-N} - E_{GB-H} - (E_{bulk}^{N} - E_{bulk}) \qquad (6)$$

where, E_{GB-H-N} and E_{GB-H} are the potential energies of the GB structure with H atom and with and without N atom at the interstitial site. E_{bulk}^{N} and E_{bulk} are the potential

energies of a single crystal bulk Nb simulation cell with and without interstitial nitrogen atom. A positive value of co-segregation energy represents that nitrogen suppresses segregation of hydrogen whereas a negative value of E_{co-seg} indicates that co-segregation of both hydrogen and nitrogen is energetically favorable at the grain boundary. In case of Σ5(210) GB, the hydrogen atom is present at its most stable interstitial site (P1) and the nitrogen atom is first added its most stable P3 site and then at the P2 interstitial site. As shown in table 4, the co-segregation energy is negative when N atom is added to P3 site whereas E_{co-seg} is positive (0.106eV) when N atom is present at the P2 site. Thus, co-segregation of hydrogen and nitrogen was favorable when nitrogen was present at P3 site whereas the co-segregation was no longer energetically favorable when nitrogen was present at P2 site.

Table 4: Co-segregation energy (E_{co-seg}, eV) of hydrogen at P1 site and nitrogen at different interstitial sites around Σ5(210) GB.

Hydrogen and nitrogen co-segregation energy at Σ5(210) GB		
Position of N	Distance b/w H & N	E_{co-seg} (eV)
P2	2.47	0.106
P3	3.75	-0.231

Similarly, for Σ5(310) GB the hydrogen atom was segregated at P1 stable interstitial site and N atom was first segregated near the P1 site and then at the P2 site. The co-segregation energy is positive when N atom is present at the P1 site whereas E_{co-seg} is

negative (-0.366eV) when N atom is present at the P2 site (Table 5). Thus, nitrogen suppressed hydrogen segregation at Σ5 STGBs in niobium but the extent of suppression gradually diminished as the distance between hydrogen and nitrogen increased and the co-segregation became energetically favorable after ~2.6 Å. This suppressing effect of nitrogen on hydrogen segregation at Σ5 STGBs is consistent with the effect of nitrogen on hydrogen binding or hydride nucleation in bulk Nb.

Table 5: Co-segregation energy (E_{co-seg}, eV) of hydrogen at P1 site and nitrogen at different interstitial sites around Σ5(310) GB.

Hydrogen and nitrogen co-segregation energy at Σ5(310) GB		
Position of N	**Distance b/w H & N**	E_{co-seg} **(eV)**
P1	2.31	0.148
P2	2.75	-0.366

4.4 Summary

In this work, first-principles calculations were employed to investigate the effect of hydrogen segregation at $1/2 \langle 111 \rangle$ screw dislocation core and Σ5 symmetric tilt grain boundaries in Nb. The screw dislocation core transformed from a non-degenerate to degenerate/hard dislocation core structure upon addition of H atom. The valence charge transfer calculations indicate towards hydride precipitation as a contributing factor to the stability of degenerate dislocation core configuration upon addition of hydrogen. Thus, changes in local environment due to the presence of solutes like the number of neighbors

and atomic distances, and the nucleation of second phase precipitates can be the factors contributing to the stability of hard core configuration. Further, presence of hydrogen increased the energy barrier for dislocation motion leading to solute hardening and significantly altering the plastic behavior of niobium. As observed in bulk niobium, nitrogen doping was found to significantly affect hydrogen segregation at niobium grain boundaries as well. Hydrogen atom segregated favorably around the grain boundary plane in $\Sigma 5$ STGBs, however presence of nitrogen suppressed hydrogen segregation but the suppressing effect was dominant only in the proximity of nitrogen, approximately up to 2.6 Å.

CHAPTER 5

5 ROLE OF DIFFERENT LATTICE DEFECTS AND MAGNETIC FLUX TRAPPING

BEHAVIOR OF NIOBIUM

5.1 Introduction

Control of growth orientation and defect structures was identified long ago as an

important requirement for niobium single-vortex devices, which underpin many

applications in quantum logic and astrophysics(Peter, Muck, and Heiden 1993; Wildes,

Mayer, and Theis-Bröhl 2001). SRF cavities are one of the critical components to

develop high-performance particle accelerators (P. Garg et al. 2018; Pashupati Dhakal,

Ciovati, and Myneni 2017). The surface resistance (R_S) defines the power dissipation at

the inner surface of SRF cavity and comprises of two terms: the Bardeen-Cooper-

Schrieffer (BCS) resistance R_{BCS} and the residual surface resistance R_{res}(Alex Gurevich

2012; A Grassellino and A Romanenko and D Sergatskov and O Melnychuk and Y

Trenikhina and A Crawford and A Rowe and M Wong and T Khabiboulline and F

Barkov 2013). The R_{BCS} term originates from microwave absorption by thermally excited

quasiparticles and becomes zero as T → 0 because quasiparticles excitation ceases at 0

K(Kubo 2016). Conversely, R_{res} remains finite as T → 0 and arises from magnetic flux

trapping, normal conducting precipitates, sub-gap, impurities, defects etc., which depend

on the material properties(A. Gurevich and Ciovati 2013; Pashupati Dhakal, Ciovati, and

Myneni 2012). The major contribution to R_{res} stems from magnetic flux trapping at

defects during cavity cooling (Huang, Kubo, and Geng 2016; Benvenuti et al. 1999) and

therefore it is critical to reduce the trapped magnetic flux in order to improve Q_O of niobium SRF cavities.

Electromagnetic fields accelerate the charged particles inside the SRF cavities being operated in the Meissner state such that the external magnetic field is completely expelled from the superconducting material(Meissner and Ochsenfeld 1933). But the presence of material imperfections like defects, impurities etc. can suppress the expulsion of magnetic field and pin the field inside the material even after the externally applied field is removed(Knobloch and Padamsee 1997; Vallet et al. 1992). The trapped field is present in the form of quantized vortices which have a normal conducting core, where unpaired electrons cause Ohmic resistance and contribute to R_{res} thereby decreasing the cavity quality factor(Aull, Kugeler, and Knobloch 2012). Thus, flux trapping at the crystal lattice imperfections like dislocations and grain boundaries contribute to R_{res} and significantly degrade the performance of niobium for SRF applications(Ford, Cooley, and Seidman 2013b; Knobloch 2003; P Dhakal et al. 2013; Khanra 1975; P. J. Lee et al. 2006).

Aull *et al.*(Aull, Kugeler, and Knobloch 2012) reported nearly 100% flux trapping in polycrystalline niobium which decreased to ~41% in heat treated and polished single crystal niobium samples. Flux pinning at the grain boundaries in niobium bi-crystals was found to be dependent upon the grain boundary tilt axis and attributed to the electron-scattering mechanism(DasGupta et al. 1978; Cai, Chou, and Gupta 1987). Additionally, a non-uniform distribution of dislocations was also observed to interact with and trap flux lines in cold rolled polycrystalline niobium(Narlikar and Dew-Hughes 1964). Flux

trapping due to hydride segregation along the low angle grain boundaries has also been reported during magneto-optical imaging analysis(Sung et al. 2017). In general, the pinning mechanism of defects for a given superconducting material can be classified into the condensation energy interaction, the elastic interaction, the magnetic interaction and the kinetic energy interaction(Matsushita 2007; Ullmaier et al. 1970; Antoine 2018). Several theories such as crystal-anisotropy of the upper critical field(Khanra 1975; Campbell and Evetts 1972; Vinnikov, Zasavitskii, and Moskvin 1982), electron-scattering at the grain boundary (Cai, Chou, and Gupta 1987), elastic interactions between the dislocations present at the grain boundaries and the flux line lattice (Pande and Suenaga 1976) etc. had been proposed to explain the flux trapping at defects. However, mechanism(s) underlying the flux pinning at defects has not been unequivocally established since the applicability of various flux pinning theories at defect has not been determined for a wide variety of samples.

This work marks the first attempt to understand the influence of lattice defects, i.e., vacancies, dislocations and grain boundaries on magnetic flux trapping in niobium within the first-principles framework. Equilibrium structures for different defects were obtained using molecular dynamics and density functional theory calculations. The external magnetic field was simulated using the all-electron full-potential linearized augmented plane wave code to analyze the flux trapping tendencies of different defects.. Further, grain boundary character was found to play a crucial role on the flux trapping behavior since the trapped flux was observed to vary with the grain boundary mis-orientation angle. To determine the mechanisms underlying the interactions between external

magnetic field and different defects, the electronic structure of defects was analyzed using electronic density of states and Bader charge analysis within first-principles framework. Difference in the electronic structure of defects as compared to body centered cubic niobium indicates to a potential magnetic state in the presence of an external magnetic field thereby promoting flux trapping at defects and disrupting the superconductivity in niobium. Such information will provide guidance for developing processing techniques to minimize undesirable defect density and improve the quality factor of niobium SRF cavities.

5.2 Computational Methodology

The first-principles calculations were performed within density functional theory (DFT) framework using Vienna Ab-initio Simulation Package (VASP) (Georg Kresse and Hafner 1993; G. Kresse and Hafner 1994), with Perdew-Burke-Ernzerhof (PBE)(Georg Kresse and Furthmüller 1996; Blöchl 1994) exchange-correlation functional.

5.2.1 Point Defects

A supercell approach was used to model a metal vacancy in bulk crystal and determine the parameters relevant for vacancy formation. A niobium atom was removed from its lattice site in a $2 \times 2 \times 2$ body centered cubic (bcc) niobium supercell (16 niobium atoms) to represent a vacancy concentration of 6.25 at% and calculate the vacancy formation energy. The k point mesh of $13 \times 13 \times 13$ was selected based on convergence studies and the atoms were relaxed with a force and energy convergence

criteria of 0.01 eVÅ^{-1} and 10^{-6} eV respectively. The atoms were allowed to relax in all directions while maintaining periodic boundary conditions and relaxing the supercell volume and shape. The vacancy formation energy (ΔE_{vac}) is calculated using:

$$\Delta E_{vac} = E_{(n-1)} - \frac{n-1}{n} E_n \qquad (7)$$

where E_{n-1} denotes the total energy of the cell containing a vacancy, n is the number of atoms in the supercell and E_n represents the total energy of the perfect supercell without any vacancy (Mattsson and Mattsson 2002; Wolverton 2007). The interactions between the vacancies across the periodic boundaries were minimized since the vacancy formation energy for 16 atoms and 24 atoms niobium supercell converged within 0.02 eV. The calculated vacancy formation energy value of 2.51 eV was found to be in good agreement with the reported experimental and theoretical values(Korhonen, Puska, and Nieminen 1995; Korzhavyi et al. 1999).

5.2.2 Planar Defects

Three symmetric tilt grain boundary (STGB) systems (<100>, <110>, and <111>) and a non-symmetric tilt grain boundary sample were created in LAMMPS with semi-empirical EAM potential for niobium as explained in Chapter 4. The grain boundary energy (E_{gb}) was calculated as the difference between the energy of the GB simulation cell with n atoms (E_n) and the cohesive energy of niobium atoms (E_{coh}) per unit area of the grain boundary plane (A).

$$E_{gb} = \frac{E_n - n*E_{coh}}{2A} \qquad (8)$$

The expression is divided by 2 due to the two interfaces in the grain boundary simulation cell. The GB energy as a function of the mis-orientation angle for ⟨100⟩, ⟨110⟩ and ⟨111⟩ tilt axes of niobium is shown in figure 16a. Furthermore, figure 16b shows the variation of grain boundary energy with mis-orientation angle mapped onto a stereographic triangle with the convention for representing cubic metals. The vertices of the triangle represent the three principal orientation of the cubic system. The GB mis-orientation was defined by the polar/azimuthal angles and the GB energy was represented by the color contour. The color bar corresponds to the GB energies between 600 mJ/m^2 and 1400 mJ/m^2 which represents the GB database for the three symmetric tilt axes. The observed trends of the grain boundary energy with mis-orientation angle are comparable to the previously reported values (Singh and Parashar 2018).
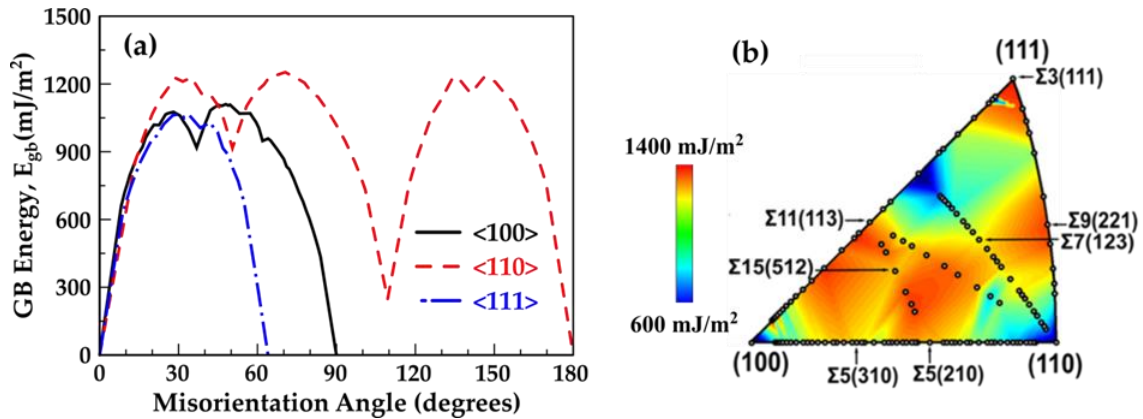
Figure 16: Grain boundary energy (E_{gb}) represented as a function of (a) mis-orientation angle and (b) polar and azimuthal angles for <100>, <110> and <111> STGBs in Nb. Grain boundaries with minimum energy can be identified from the standard stereographic triangle with the color bar.

56

Due to the size constraints of first-principles methods, smaller supercells with one periodic length along the GB and few atomic planes (25-35 atomic planes) perpendicular to the GB plane were obtained from the bi-crystal simulation cell of MD calculations. The smaller supercells for different grain boundaries were relaxed within DFT framework. The k point mesh for each of the GB supercells was selected, after extensive k point sampling, based on the convergence studies (see table A1 in appendix) and the atoms were relaxed with 10^{-6} eV energy tolerance while maintaining a constant volume and shape of the supercells. The GB supercells with negligible grain boundary interactions across the periodic images were selected for further flux trapping studies.

5.2.3 External Magnetic Field

The state-of the-art all-electron full-potential linearized augmented plane wave (FP-LAPW) code was used to analyze the defect interaction with external magnetic field(Sharma, Dewhurst, et al. 2007; Sharma, Pittalis, et al. 2007). The FP-LAPW code formulation is based on the Kohn-Sham equations for external field in a two-step variational process(Sharma, Dewhurst, et al. 2007; Jin et al. 2015; Yang, Yue, and Hu 2016). In the first-variational step a Hamiltonian ($\widehat{H}$) containing only the scalar potential and **E** field is constructed

$$\widehat{H} = \widehat{T}_s + \widehat{V}_{ext} + \boldsymbol{E}.\hat{\boldsymbol{r}} + \widehat{V}_{xc} \tag{9}$$

and diagonalised with $\widehat{H}|\phi_i\rangle = \varepsilon_i|\phi_i\rangle$. $\widehat{T}_s$ is the kinetic energy operator, $\widehat{V}_{ext}$ is the external potential operator, $\widehat{V}_{xc}$ is the exchange-correlation (XC) potential operator and ε_i is the orbital energy of the corresponding Kohn–Sham orbital, ϕ_i (Sharma, Dewhurst, et

al. 2007). In the second-variational step, the magnetic fields, spin-orbit coupling and **A** field are added using the first-variational step as a basis

$$H_{ij} = \varepsilon_i \delta_{ij} + \langle \phi_i | \boldsymbol{\sigma} \cdot (\widehat{\boldsymbol{B}}_{ext} + \widehat{\boldsymbol{B}}_{xc}) + \boldsymbol{\sigma} \cdot \widehat{L} + \boldsymbol{A} \cdot \widehat{\nabla} | \phi_i \rangle \tag{10}$$

where B_{xc} is the exchange-correlation magnetic field. Instead of the usual approach of separating the Kohn-Sham equations into spin-up and spin-down orbitals, densities and potentials, the FP-LAPW code formulation treats magnetism as non-collinear for which the basic variables are the scalar density $\rho(r)$ and the magnetization vector field m(r). An external magnetic field ($B_{ext} = 171.5$ mT) was applied along different defects below superconducting transition temperature of niobium ($T_c = 9.25$ K), during the flux trapping calculations. Niobium is treated as paramagnetic in nature below T_c in the FP-LAPW code formulation. Periodic boundary conditions were maintained along all directions. The applied field was reduced by a factor of 0.85 after each ionic step such that the applied field is infinitesimal i.e. effectively zero at the end of all the steps. The factor of 0.85 for decrease in applied field was selected based on the convergence studies to eliminate any sudden change in the applied field and to optimize the use of computational resources. The augmented plane wave basis was used to accurately compute the effective potential under external magnetic field without local discontinuities in the XC potentials introduced by functional approximations. The Fermi-Dirac smearing method was used for a smooth approximation of the Dirac delta function needed to compute the occupancies of the Kohn-Sham states. The self-consistent loop is converged when the total energy is smaller than 10^{-3} eV and the root mean square change in Kohn-Sham potential and magnetic field is smaller than 10^{-3} Tesla.

58

5.3 Results

The first step towards understanding the flux trapping behavior at different defects is to determine the effect of external magnetic field on pure single crystal niobium. It is very well known that niobium is paramagnetic above its superconducting transition temperature and superconducting in nature below T_c. Hence, there is no flux trapping in niobium and the externally applied magnetic field is completely expelled from the material as also observed in our flux trapping simulations. Next, we examine the effect of point defects, line defects and planar defects on flux trapping.

5.3.1 Flux Trapping at Point and Line Defects in Niobium

To examine the role of point defects on magnetic flux trapping, the external magnetic field was applied perpendicular to (100) plane of niobium supercell with a vacancy concentration of 6.25 at%. A very small remnant magnetic moment of $0.005\mu_B$ was observed in the bcc supercell with a vacancy concentration of 6.25 at% after the externally applied magnetic field was removed. The magnitude of remnant magnetic moment was independent of the direction of applied field due to symmetry and periodic boundary conditions. The trapped or residual magnetic flux density (B_r) due to the presence of defects was calculated from the remnant magnetic moment (M) as:

$$B_r = \frac{M\mu_0}{V} \tag{11}$$

where V is the volume of supercell and μ_0 is the permeability of vacuum ($4\pi \times 10^{-7}$ H/m). Thus, the trapped flux density was found to be 0.19 mT for niobium supercell with a point defect concentration of 6.25 at%.

Further, the effect of line defects on magnetic flux trapping behavior of niobium was investigated using the screw dislocation dipole structure. The external magnetic field was applied along $\vec{c}_1$ direction of the supercell to examine the flux trapping behavior of dislocations. After the externally applied magnetic field was removed, the magnitude of remnant magnetic moment was observed to be $1.00\mu_B$. Thus, the trapped or residual magnetic flux density due to the dislocation dipole structure of supercell volume 2481.2 Å^3 was found to be 4.70 mT using Eq. 11. The red atoms of the upward and downward triangles in the (111) plane represent the dislocation dipoles whereas the blue colored atoms represent bcc niobium.
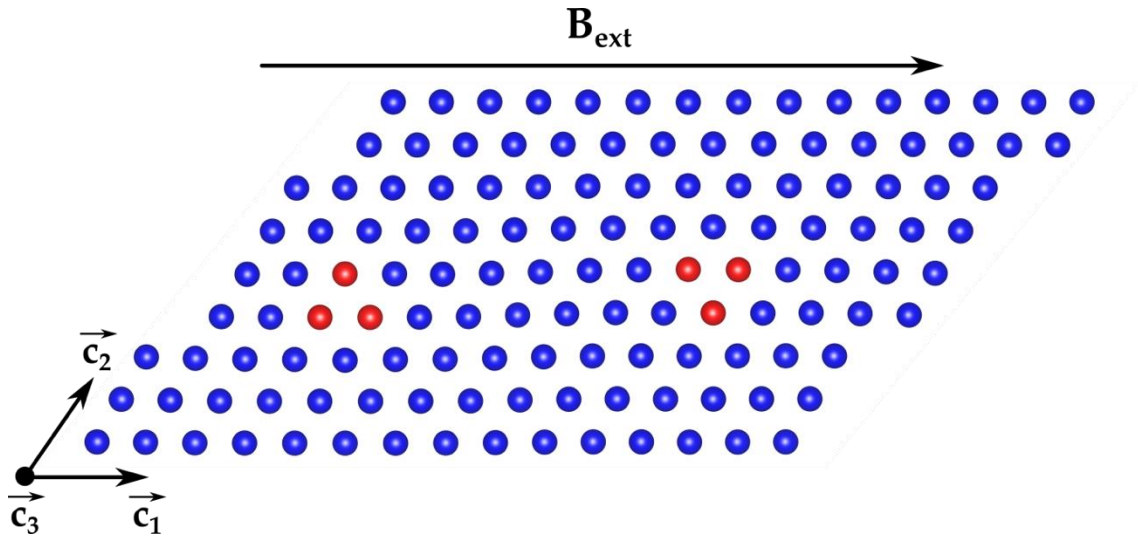
Figure 17: Screw dislocation core structure on (111) plane in bcc niobium. The atoms are colored according to common neighbor analysis such that dislocation core atoms are red and bcc atoms are blue.

5.3.2 Flux Trapping at Planar Defects in Niobium

The role of planar defects on magnetic flux trapping in niobium was investigated by applying the external magnetic field along the GB plane parallel to x-axis of the simulation cell, as illustrated in figure 17. The applied field decreased gradually to zero at the end of all self-consistent loops and a residual magnetic moment was observed in the GB simulation cells. For instance, a residual magnetic moment of $0.54\mu_B$ was observed in the $\Sigma5$ (210) grain boundary. The magnitude of trapped flux was calculated from the residual moment and volume of the simulation cell using Eq. 11, given in table 6. Among different GBs studied here, the trapped flux was minimum for the highly symmetric $\Sigma1$ (101) grain boundary ($\theta = 60°$) whereas maximum flux was trapped at $\Sigma3$ (111) grain boundary. Overall, the magnitude of trapped flux at different grain boundaries was found to vary from 2 mT to 20 mT. These results are in good agreement with the cold rolled niobium bi-crystal samples where premature flux penetration was observed to occur at 8-20 mT(P. Lee et al. 2006).
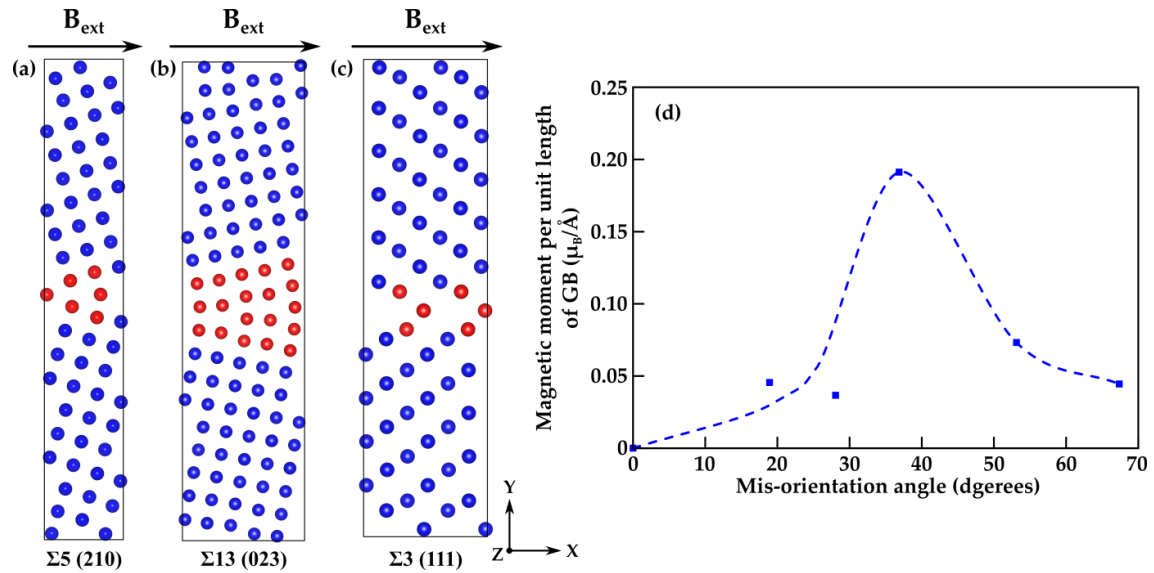
Figure 18: Schematic of externally applied magnetic field (B$_{ext}$) along the grain boundary plane of (c) Σ5 (210), (d) Σ13 (023) and (e) Σ3 (111) grain boundaries in Nb. (d) The remnant magnetic moment per unit periodic length of GB as a function of the GB mis-orientation angle for <100> symmetric tilt grain boundaries. Blue and red colored solid circles represent body-centered cubic and grain boundary atomic structures, respectively, obtained from the common neighbor analysis in Ovito.

The grain boundary character was found to play a significant role in their flux trapping behavior. The remnant magnetic moment per unit periodic length of the GB was observed to increase with increase in GB mis-orientation angle approximately up to θ = 40° for the GBs part of the <100> STGB system. However, above 40° the magnetic moment per unit periodic length of the GB decreased gradually, as shown in figure 18.

Table 6: The magnitude of trapped magnetic flux at different grain boundaries in niobium

Flux trapping at Nb grain boundaries			
Grain Boundary	Mis-orientation angle	Magnetic moment (μ_B)	Trapped Flux (mT)
$\Sigma 5$ (210)	53.13°	0.54	5.74
$\Sigma 5$ (310)	36.87°	2.00	15.17
$\Sigma 13$ (023)	67.38°	0.53	3.25
$\Sigma 37$ (016)	18.92°	0.92	4.06
$\Sigma 17$ (014)	28.07°	0.50	4.66
$\Sigma 3$ (111)	70.53°	2.00	19.38
$\Sigma 1$ (101)	60°	0.22	1.98

Next, the Voronoi tessellation method(Du, Faber, and Gunzburger 1999) was used to construct a polycrystalline sample of niobium containing grains of identical shape and size with [110] tilt axis to study flux trapping behavior of a non-symmetric tilt grain boundary (figure 19a) (Bhatia, Mathaudhu, and Solanki 2015; Millett et al. 2008). The sample was relaxed, within LAMMPS framework, to uniformly distribute the excess free energy in the whole system while maintaining periodic boundary conditions. The non-symmetric tilt grain boundary was translated into first-principles framework using a bi-crystal simulation cell with one periodic length along GB (figure 19b) owing to the size limitations of first-principles method. The bi-crystal simulation cell was relaxed using DFT methods and further examined for flux trapping studies. The magnetic field was applied along x-axis, parallel to the GB plane (figure 19b) and gradually reduced to zero

at the end of self-consistent loops. A residual magnetic moment of $0.499\mu_B$ was observed

corresponding to 2.5mT of trapped flux at the [110] non-symmetric tilt grain boundary.
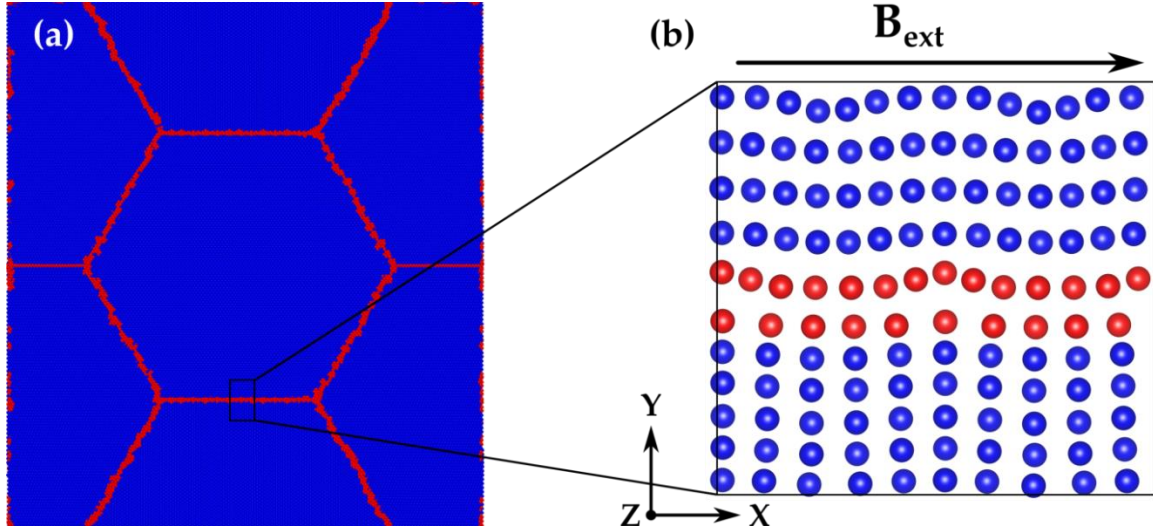
Figure 19: (a) An equilibrated polycrystalline sample constructed using the Voronoi tessellation consisting of non-symmetric tilt grain boundaries and (b) schematic of externally applied magnetic field (B_{ext}) along the grain boundary plane of a non-symmetric tilt grain boundary in Nb. Blue and red colored solid circles represent body-centered cubic and grain boundary atomic structures, respectively, obtained from the common neighbor analysis. The z-axis is aligned along [110] direction.

5.3.3 Electronic Structure Analysis

An external magnetic field generally engages with both the electron spin and the electronic orbital current in a metallic system. Further, the interaction of magnetic field with different defects can lead to crystalline magnetic anisotropy, magneto-volume effects and difference in electromagnetic state between the grain boundary and the grain interior(Watanabe et al. 2006). Therefore, examination of the electronic structure can play a crucial role in elucidating the underlying mechanisms associated with flux trapping

behavior of defects. Electronic density of states and Bader charge analysis were performed using VASP to study the electronic structure of different defects in their equilibrium condition before the external magnetic field was applied.

5.3.3.1 Density of States (DOS)

Figure 20 shows the electronic density of states for bcc niobium, niobium with dislocation dipole structure and niobium bi-crystals with symmetric tilt grain boundaries. The DOS curve below the Fermi level (0 eV) represents the occupied states (bonding states); whereas, the curve above the Fermi level represents the unoccupied states (antibonding states)(P. Garg, Adlakha, and Solanki 2018; P. Garg et al. 2017). All the electronic density of states calculations were performed using the tetrahedron smearing method with Blöchl corrections within DFT framework(Blöchl, Jepsen, and Andersen 1994). The orbital decomposed DOS curves of bcc niobium show d-orbital splitting into two irreducible collective orbital representations t_{2g} and e_g (figure 20a). The occupied t_{2g} bands (d_{xy}, d_{yz} and d_{zx}) sit lower in energy than the e_g orbital ($d_{x^2-y^2}$ and d_{z^2}), while the opposite is true in the unoccupied states, as is expected for octahedral coordinated centers and reported in literature (Pulkit Garg et al. 2018; Ford, Zapol, and Cooley 2015; Grad et al. 2000). In contrast to un-defected niobium, the degeneracy of t_{2g} and e_g states is lifted due to the presence of defects i.e. dislocations and grain boundaries. The presence of antibonding peak around 1eV in the DOS curve of $Nb_{15}Vac_1$ indicates to reduction in bond strength around the point defect thus decreasing the structural and electronic stability of niobium with vacancy as compared to bcc niobium (figure 20b).

65

In the presence of dislocation dipole structures the d states energies re-order to new iso-energetic d_{xy} and $d_{x^2-y^2}$ states, d_{yz} and d_{zx} states, and a non-degenerate d_{z^2} state (figure 20c). The total DOS curve for niobium with dislocation dipole structure is in good agreement with the reported DOS curve (L. Dezerald et al. 2014). Further, in case of $\Sigma 5$ (310) symmetric tilt grain boundary the degeneracy of e_g states is further lifted between the $d_{x^2-y^2}$ and d_{z^2} states (Fig. 5e). Additionally, the initial degeneracy of t_{2g} states is reduced since only d_{yz} and d_{zx} states overlap with each other while d_{xy} is non-degenerate. Similar non-degenerate splitting of d states is observed in other grain boundaries; however the extent of non-degeneracy is different in different grain boundaries (figure 20d-j). Thus, the degeneracy of the valence and conduction band *d*-states is removed due to the localized bonding distortion at the defects. The partial or complete removal of the d state degeneracy is determined by the extent and nature of asymmetry introduced by the defect(G. Lucovsky et al. 2005). Therefore, changes in local coordination of atoms at the defects trigger splitting of orbitals, thereby enhancing tendency of niobium towards magnetism, which can lead to a magnetic states at defects in the presence of an external magnetic field.
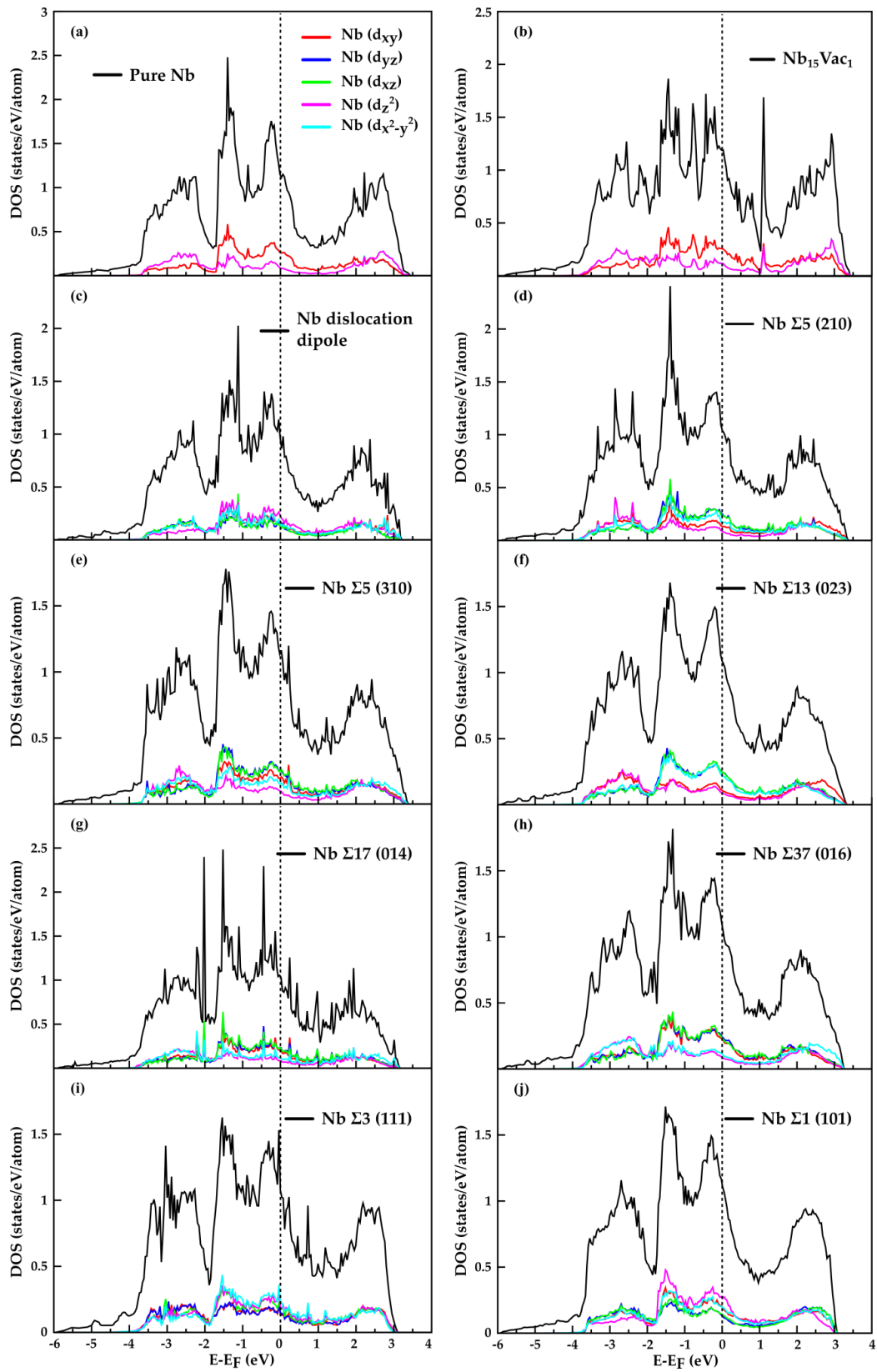
Figure 20: Total and orbital decomposed density of states curves for (a) bcc niobium, (b) niobium with 6.25 at% of vacancy, (c) screw dislocation dipole, (d)-(h) <100> family of STGBs, (i) <110> family of STGB and (j) <111> family of STGB.

5.3.3.2 Bader Charge Analysis

The response of a material to an external source depends on the nature of atomic bonding between the atoms which is associated with the atomic charge distribution(P. Garg, Bhatia, and Solanki 2019; P. Garg, Adlakha, and Solanki 2019). Bader's quantum theory of atoms in molecules defines atoms, bonds and chemical structure of the material as a function of the electron density in the system(Sanville et al. 2007; Carballo-Córdova et al. 2019). The charge obtained from the first-principles calculations was separated and determined for each atom using the Bader charge analysis. A sufficient number of core electrons were included (6 *4p*, 4 *4d* and 1 *5s* electrons) to obtain correct results from Bader charge analysis. Figure 21 shows the Bader charge around niobium atoms for different defects. A significant amount of charge accumulation (0.1 e) and reduction (0.1 e) was observed in niobium with 6.25 at% vacancy as a result of decreased atomic coordination number which leads to reduced hybridization between the electrons (figure 21a). Charge redistribution around the dislocation dipole core structures is considerably lower ($\pm$0.03) due to the symmetric nature of the line defect (figure 21b). Considerable charge redistribution varying from 0.05e to 0.25e was observed in the bi-crystals especially around the grain boundary atoms (figure 21c-i). For example, in case of Σ13(023) STGB some of the grain boundary atoms have accumulated Bader charge of 11.12e (red atoms) while some GB atoms have depleted charge of 10.90e (blue atoms) as

compared to the Nb atoms away from the GB which have a Bader charge of 11.00 e (green atoms) same as bcc Nb. Thus valence charge transfer around the defects can lead to localization of electrons, leading to their significantly different magnetic properties as compared to the bulk and enhancing tendency of niobium towards magnetism in the presence of external magnetic field.

(a)

(b)

(c) Σ5 (210)

(d) Σ5 (310)

(e) Σ13 (023)

(f) Σ37 (016)

(g) Σ17 (014)

(h) Σ3 (111)

(i) Σ1 (101)

70
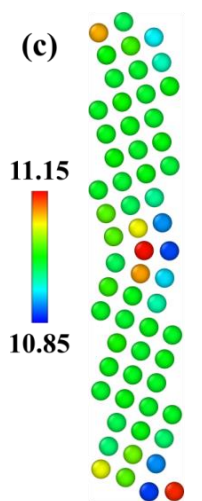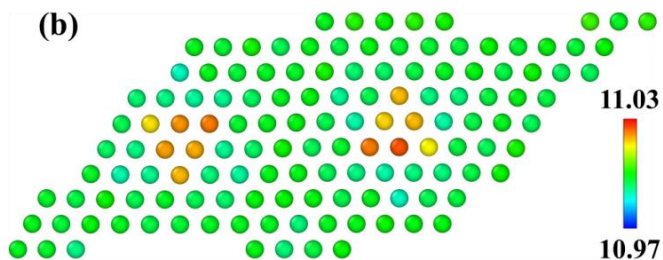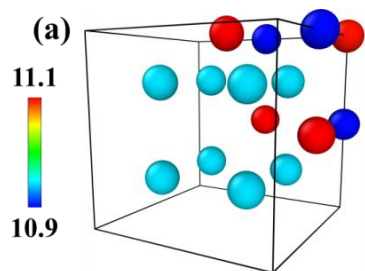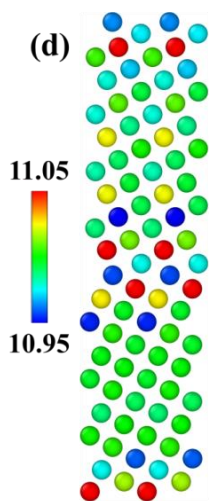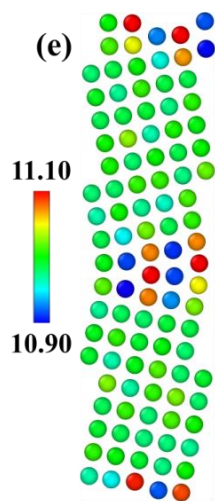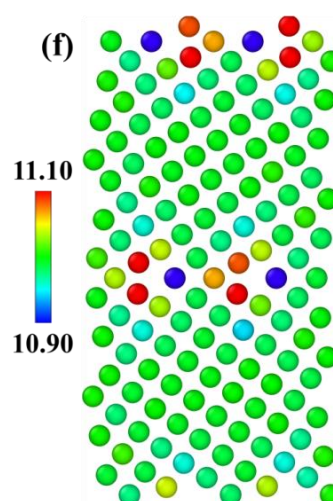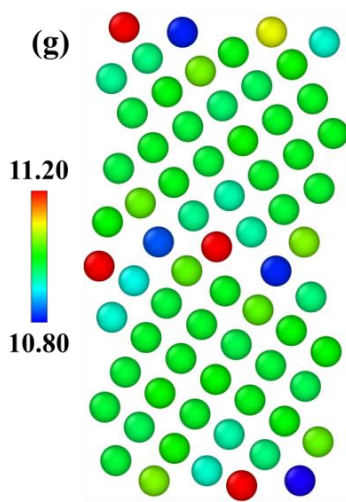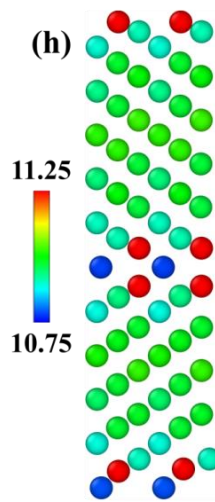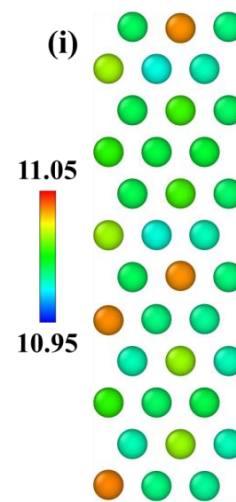
Figure 21: Bader charge analysis for (a) bcc niobium with 6.25 at% of vacancy, (b) screw dislocation dipole, (c)-(g) <100> family of STGBs, (h) <110> family and (i) <111> family of STGB. The atoms are colored according to the Bader charge on each atom.

Next, the partial and orbital decomposed DOS for different Bader atoms of all the grain boundaries studied here were obtained to determine the localized effect of planar defects on flux trapping behavior. As an illustration, the orbital and partial DOS are shown for the Bader atoms of Σ3 (111) GB, the grain boundary with highest magnetic moment and trapped flux (figure 22). Σ3 (111) GB in figure 22 (a) is colored based on the Bader charge analysis, where green atoms (11.0 e) represent the bulk niobium atoms away from GB and the red (11.25 e) and blue atoms (10.75 e) represent the GB atoms with accumulated and depleted charge respectively. The partial DOS for the niobium atoms away from the GB, and at the grain boundary with accumulated and depleted charge respectively were found to be different from each other (figure 22b). The accumulated electrons occupy $d_{x^2-y^2}$ orbitals in addition to d_{yz} and d_{xy} orbitals already occupied by the original $4d$ electrons (figure 22d). In bulk Nb atoms, localization of d orbitals was observed due to $d_{x^2-y^2}$ and d_{z^2} around -1.5 eV (figure 22c). However, a stronger localization of d orbitals was observed in the grain boundary atoms with accumulated Bader charge from the additional peaks of d_{yz} and d_{zx} orbitals around -3.5 eV (figure 22d). Whereas, the delocalization contribution was reflected from the smoother DOS curve of the GB atoms with depleted Bader charge (figure 22e). The spin-up and spin-down DOS curves are symmetric for the grain boundary atoms as well as for the atoms away from grain boundary and there is no net magnetic moment in the bi-

crystal simulation cell. However, the accumulation and depletion of charge at the grain boundary atoms can enhance non-paramagnetism in niobium, leading to a magnetized state when the material is exposed to an external magnetic field. Such non-paramagnetic behavior has been observed in niobium where the material underwent transition from a non-magnetic state to a low-spin antiferromagnetic state to a high-spin ferromagnetic state upon lattice expansion(Jani, Brener, and Callaway 1988; Moruzzi and Marcus 1990).
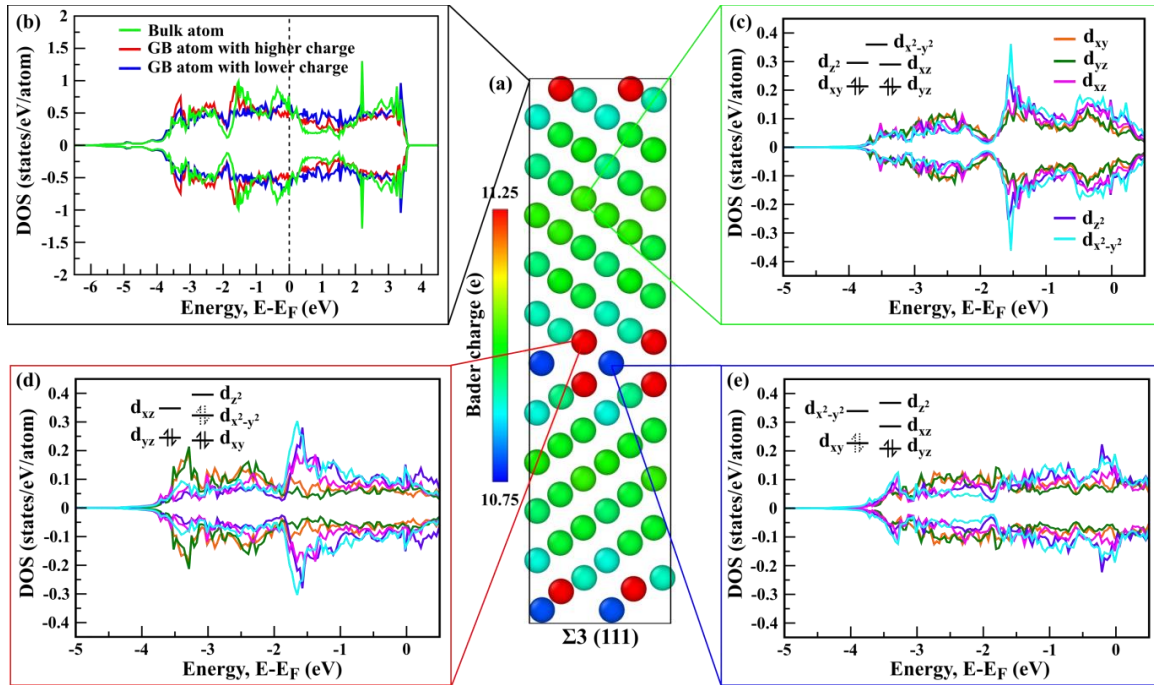
Figure 22: (a) Bader charge analysis for Σ3 (111) STGB in niobium. Atoms are colored according to the Bader charge on each atom. (b) Partial DOS curves for different atoms selected based on Bader charge analysis of Σ3 (111) STGB. Orbital decomposed DOS curves for (c) bulk atom, grain boundary atom with charge (d) accumulation and (e) depletion respectively below the Fermi level in Σ3 (111) STGB.

5.4 Summary

In summary, the present work provides a theoretical point of view to understand the interaction of external magnetic field with different lattice defects like dislocations and grain boundaries and its effect on the magnetic properties of niobium via first-principles methods. Equilibrium defect structures were obtained using DFT methods and the external magnetic field was applied within the FP-LAPW code formulation. The magnitude of trapped flux at a vacancy was found to be significantly smaller as compared to the dislocation dipole and grain boundaries with grain boundary character playing a significant role on flux trapping. Further, the electronic structure of defects was determined using density of states and Bader charge analysis within first-principles framework to illustrate the underlying mechanism of interactions between external magnetic field and defects. Charge redistribution and splitting of d states in the defect region suggest towards their significantly different magnetic properties and non-paramagnetic behavior as compared to bcc niobium. Different electronic structure of defects as compared to bulk niobium indicates to a magnetized state in the presence of an external magnetic field thereby promoting flux trapping at defects.

CHAPTER 6

6 SUMMARY AND FUTURE WORK

Niobium is the primary material for fabricating superconducting radio frequency cavities for particle accelerators owing to its superconducting properties, extremely low surface resistance to charge carriers and good ductility and malleability. However, the effectiveness of niobium is significantly reduced due to the presence of impurities like hydrogen which nucleate non-superconducting hydride precipitates or due to the development of a non-superconducting region upon magnetic flux trapping at the lattice defects. In this dissertation, first-principles methods were implemented to systematically investigate the underlying mechanisms associated with the observed low hydrogen and hydride concentration in nitrogen treated niobium. The firs-principles calculations were also implemented for the first time to gain a theoretical perspective about the experimental observation that lattice defects like dislocations and grain boundaries are effective sites for trapping magnetic flux in high-purity superconducting niobium. This understanding will aid in development of processing techniques to minimize undesirable impurity and defect density to improve the quality factor of niobium for SRF cavities. The several insights gained from this dissertation include:

(i)   Addition of nitrogen significantly affects hydrogen binding in niobium. In the presence of nitrogen, hydrogen binding in niobium was suppressed but the suppressing effect was dominant only in the proximity of nitrogen, approximately up to a distance of 2.5 Å away from nitrogen.

(ii)   The density of states and valence charge transfer calculations showed that the suppressing effect of nitrogen on hydrogen binding in niobium was due to the weakening of covalent bonds between the niobium and hydrogen atom.

(iii)   Nitrogen doping affected kinetic stability of hydrogen in niobium since the minimum energy path for hydrogen diffusion from one tetrahedral site to another was altered, leading to a notable increase in the activation energy barrier for hydrogen diffusion.

(iv)   The $\beta - NbH$ precipitate became energetically unstable near a nitrogen atom in the niobium matrix since the niobium hydrogen covalent bonding was disrupted by nitrogen. Thus, introduction of nitrogen into the surface of niobium cavities significantly decreased the thermodynamic and kinetic stability of hydrogen in niobium and consequently reduced the likelihood of hydride precipitation as also demonstrated experimentally.

(v)   The screw dislocation core was observed to transform from a non-degenerate to degenerate dislocation core due to the presence of hydrogen. The valence charge transfer calculations indicated towards hydride precipitation as a contributing factor to the stability of degenerate dislocation core configuration upon addition of hydrogen. Further, presence of hydrogen increased the energy barrier for dislocation motion leading to solute hardening and significantly altering the plastic behavior of niobium.

(vi)   Nitrogen doping significantly affected hydrogen segregation at niobium grain boundaries, however the suppressing effect of nitrogen on hydrogen segregation was dominant only in the proximity of nitrogen (~2.6 Å).

(vii) Equilibrium defect structures were obtained using first-principles methods and full-potential linear augmented plane-wave methods were used to analyze the effects of magnetic field on the superconducting state surrounding these defects.

(viii) A considerable amount of trapped flux was obtained at the dislocation core and grain boundaries in niobium which can be attributed to significantly different electronic structure of defects as compared to bulk niobium.

(ix)   Electronic structure calculations indicate that electron redistribution at defects enhances non-paramagnetic effects that perturb superconductivity, resulting in local conditions suitable for magnetic flux trapping.

Thus, hydride suppression due to the presence of nitrogen could be one of the contributing factors to the increased quality factors beyond the traditional SRF Nb recipes in cavities using this nitrogen doping recipe that are currently being produced. However, increase in quality factors in nitrogen-doped cavities has also revealed an issue of flux trapping due to the presence of impurities in bulk Nb. Therefore, controlling accumulation or depletion of charge at the defects could mitigate these tendencies and aid in improving superconductive behavior of niobium.

In the previous chapters, lattice defects have been shown as effective sites for trapping magnetic flux in high-purity superconducting niobium. The fabrication and processing of niobium SRF cavities involves plastic deformation that introduces

microstructural defects such as geometrically necessary dislocations, dislocation

entanglements, and strain localization around GBs, which can lead to increased or

decreased magnetic flux pinning at the defects, thereby affecting the residual resistance.

The first-principles studies indicate that the grain boundary character plays a significant

role on the flux trapping behavior of Nb. However, the effect of deformation on the flux

trapping behavior of defects needs to be further evaluated. The relationship between

strain fields around microstructural defects and magnetic flux trapping is not well

understood, so it is necessary to investigate the effect of deformation in Nb on flux

pinning by defect structures. Once understood, this will help identify new processing

methods to obtain an optimized microstructure for niobium cavities. Thus, first-principles

calculations can be used to investigate the flux trapping tendency of $\Sigma5(210)$ grain

boundary under uniaxial tension.
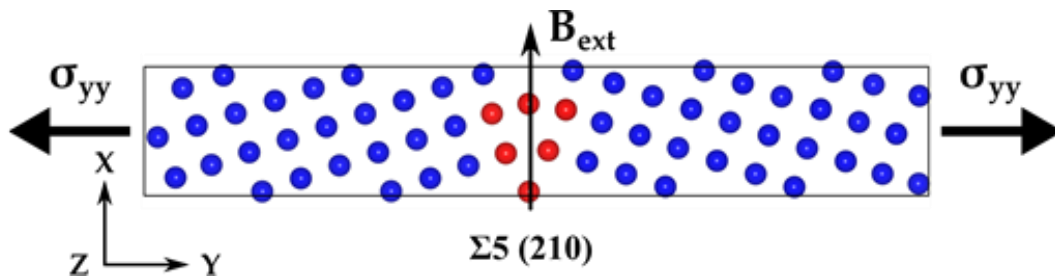
Figure 23: Schematic of external magnetic field (B_{ext}) along GB plane of $\Sigma5$ (210) GB in Nb under uniaxial tension.

Niobium does not occur in a free state in nature and is usually found together with

tantalum in the minerals like tantalite. The single grain sheets of Nb usually have an

oxide layer of mixed oxides of niobium (Nb_2O_5) and tantalum (Ta_2O_5). Hydrogen can

enter niobium whenever the natural oxide layer is removed during processing and

fabrication of cavities. The oxide layer can serve as a potential source of oxygen during bake-out in the solid solution form at the oxide-niobium interface. Thus, first-principles methods can be employed to study the relative thermodynamic stability of niobium and tantalum oxides at the Nb surface. A surface model of Nb and Nb with dilute concentrations of tantalum was built from an optimized Nb bcc crystal by cleaving a 4x4x4 supercell along the [100] direction. During surface optimizations, atomic coordinates in the bottom two-slab layers will be held fixed in their bulk positions. Although the Nb surface was oxidized through the adsorption of oxides, there was no explicit removal of metal atoms from the surface, and the local electronic density on the Nb atoms will not be precisely +5. With the help of this information, the niobium surface can be modified to support the formation of oxide layer and prevent entry of H into Nb. In principle, the anodic (reactions R1 and/or R2) and cathodic (reaction R3) reactions below represent the interaction of niobium or tantalum with oxygen leading to the formation of an oxide layer on the surface of Nb.

$$Nb \rightarrow Nb^{+5} + 5e^- \quad (R1), \quad Ta \rightarrow Ta^{+5} + 5e^- \quad (R2), \quad O_2 + 2e^- \rightarrow 2O^- \ (R3)$$
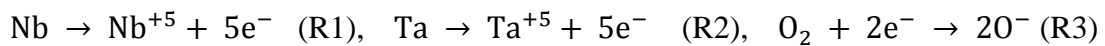
Higher thermodynamic stability of Ta oxide as compared to Nb oxide indicates that a small increase in concentration of Ta can provide a uniform Ta oxide layer on niobium surface which can prevent introduction of H into bulk during processing of niobium.
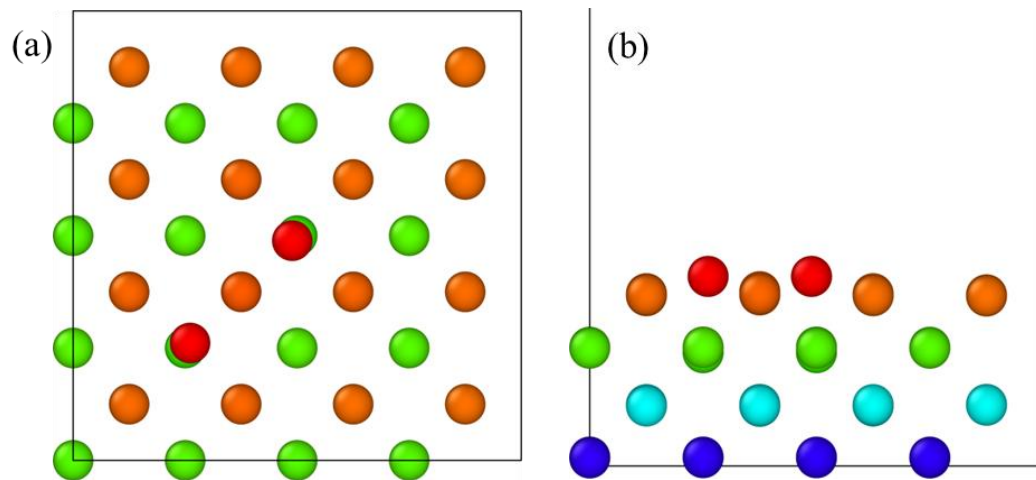
Figure 24: Adsorption of O_2 molecule on (001) surface of niobium. Atoms are colored according to their position in [001] direction. Oxygen atoms are red in color.

REFERENCES

A Grassellino and A Romanenko and D Sergatskov and O Melnychuk and Y Trenikhina and A Crawford and A Rowe and M Wong and T Khabiboulline and F Barkov. 2013. "Nitrogen and Argon Doping of Niobium for Superconducting Radio Frequency Cavities: A Pathway to Highly Efficient Accelerating Structures." *Superconductor Science and Technology* 26 (10): 102001.

A Romanenko and L V Goncharova. 2011. "Elastic Recoil Detection Studies of Near-Surface Hydrogen in Cavity-Grade Niobium." *Superconductor Science and Technology* 24 (10): 105017.

Aboud, Shela, and Jennifer Wilcox. 2010. "A Density Functional Theory Study of the Charge State of Hydrogen in Metal Hydrides." *The Journal of Physical Chemistry C* 114 (24): 10978–85. https://doi.org/10.1021/jp911811r.

Adlakha, I., M.A. Bhatia, M.A. Tschopp, and K.N. Solanki. 2014. "Atomic Scale Investigation of Grain Boundary Structure Role on Intergranular Deformation in Aluminium." *Philosophical Magazine* 94 (30): 3445–66. https://doi.org/10.1080/14786435.2014.961585.

Adlakha, I., P. Garg, and K.N. Solanki. 2019. "Revealing the Atomistic Nature of Dislocation-Precipitate Interactions in Al-Cu Alloys." *Journal of Alloys and Compounds* 797 (August): 325–33. https://doi.org/10.1016/j.jallcom.2019.05.110.

Adlakha, I., M.A. Tschopp, and K.N. Solanki. 2014. "The Role of Grain Boundary Structure and Crystal Orientation on Crack Growth Asymmetry in Aluminum." *Materials Science and Engineering: A* 618 (November): 345–54. https://doi.org/10.1016/j.msea.2014.08.083.

Adlakha, Ilaksh. 2015. "Role of Defects Interactions with Embrittlement Species in Iron: A Multiscale Perspective."

Aizaz, Ahmad, Pierre Bauer, Terry L. Grimm, Neil T. Wright, and Claire Z. Antoine. 2007. "Measurements of Thermal Conductivity and Kapitza Conductance of Niobium for SRF Cavities for Various Treatments." *IEEE Transactions on Applied Superconductivity* 17 (2): 1310–13. https://doi.org/10.1109/TASC.2007.897855.

Alefeld, Georg, and Johann Völkl. 1978. "Hydrogen in Metals I-Basic Properties." In . Vol. 28.

Antoine, CZ. 2018. "Influence of Crystalline Structure on RF Dissipation in Niobium: Flux Trapping, Hydride Precipitate, Doping Behavior..." *ArXiv Preprint ArXiv:1802.07241*.

Argon, Ali S. 2008. *Strengthening Mechanisms in Crystal Plasticity. Oxford: Oxford University*. Oxford.

Aull, S., O. Kugeler, and J. Knobloch. 2012. "Trapped Magnetic Flux in Superconducting Niobium Samples." *Physical Review Special Topics - Accelerators and Beams* 15 (6): 062001.

Balachandran, S, S Chetri, P Dhakal, D Larbalestier, and P Lee. 2017. "Hydrogen Distribution and Hydride Precipitation in SRF Nb Revealed by Metallographic Techniques." In .

Barkov, F., A. Romanenko, and A. Grassellino. 2012. "Direct Observation of Hydrides Formation in Cavity-Grade Niobium." *Physical Review Special Topics - Accelerators and Beams* 15 (12). https://doi.org/10.1103/PhysRevSTAB.15.122001.

Barkov, F., A. Romanenko, Y. Trenikhina, and A. Grassellino. 2013. "Precipitation of Hydrides in High Purity Niobium after Different Treatments." *Journal of Applied Physics* 114 (16): 164904. https://doi.org/10.1063/1.4826901.

Benvenuti, C., S. Calatroni, I.E. Campisi, P. Darriulat, M.A. Peck, R. Russo, and A.-M. Valente. 1999. "Study of the Surface Resistance of Superconducting Niobium Films at 1.5 GHz." *Physica C: Superconductivity* 316 (3): 153–88. https://doi.org/10.1016/S0921-4534(99)00207-5.

Bhatia, M. A., S. Groh, and K. N. Solanki. 2014. "Atomic-Scale Investigation of Point Defects and Hydrogen-Solute Atmospheres on the Edge Dislocation Mobility in Alpha Iron." *Journal of Applied Physics* 116 (6): 064302. https://doi.org/10.1063/1.4892630.

Bhatia, M. A., S. N. Mathaudhu, and K. N. Solanki. 2015. "Atomic-Scale Investigation of Creep Behavior in Nanocrystalline Mg and Mg–Y Alloys." *Acta Materialia* 99 (October): 382–91. https://doi.org/10.1016/j.actamat.2015.07.068.

Bitzek, Erik, Pekka Koskinen, Franz Gähler, Michael Moseler, and Peter Gumbsch. 2006. "Structural Relaxation Made Simple." *Physical Review Letters* 97 (17): 170201.

Blöchl, Peter E. 1994. "Projector Augmented-Wave Method." *Physical Review B* 50 (24): 17953.

Blöchl, Peter E., Ove Jepsen, and Ole Krogh Andersen. 1994. "Improved Tetrahedron Method for Brillouin-Zone Integrations." *Physical Review B* 49 (23): 16223.

Cabrera, A. L., J. Espinosa-Gangas, Johan Jonsson-Akerman, and Ivan K. Schuller. 2002. "Kinetics of Subsurface Hydrogen Adsorbed on Niobium: Thermal Desorption Studies." *Journal of Materials Research* 17 (10): 2698–2704. https://doi.org/10.1557/JMR.2002.0390.

Cai, BC, YT Chou, and A Das Gupta. 1987. "Flux Pinning by Symmetrical Grain Boundaries in Niobium Bicrystals." *Philosophical Magazine B* 55 (1): 55–66.

Caillard, Daniel, and Jean-Luc Martins. 2003. *Thermally Activated Mechanisms in Crystal Plasticity*. Vol. 8.

Campbell, AM, and JE Evetts. 1972. "Flux Vortices and Transport Currents in Type II Superconductors." *Advances in Physics* 21 (90): 199–428.

Carballo-Córdova, DA, MT Ochoa-Lara, SF Olive-Méndez, and F Espinosa-Magaña. 2019. "First-Principles Calculations and Bader Analysis of Oxygen-Deficient Induced Magnetism in Cubic BaTiO3− x and SrTiO3− x." *Philosophical Magazine* 99 (2): 181–97.

Christian, J. W. 1983. "Some Surprising Features of the Plastic Deformation of Body-Centered Cubic Metals and Alloys." *Metallurgical Transactions A* 14 (7): 1237–56. https://doi.org/10.1007/BF02664806.

Clouet, Emmanuel, Lisa Ventelon, and F. Willaime. 2009. "Dislocation Core Energies and Core Fields from First Principles." *Physical Review Letters* 102 (5): 055502. https://doi.org/10.1103/PhysRevLett.102.055502.

Cottrell, A. H. 1948. "Report on Strength of Solids." *The Physical Society* 30.

DasGupta, A, CC Koch, DM Kroeger, and YT Chou. 1978. "Flux Pinning by Grain Boundaries in Niobium Bicrystals." *Philosophical Magazine B* 38 (4): 367–80.

Dezerald, L., Lisa Ventelon, E. Clouet, C. Denoual, D. Rodney, and F. Willaime. 2014. "*Ab Initio* Modeling of the Two-Dimensional Energy Landscape of Screw Dislocations in Bcc Transition Metals." *Physical Review B* 89 (2). https://doi.org/10.1103/PhysRevB.89.024104.

Dezerald, Lucile, David Rodney, Emmanuel Clouet, Lisa Ventelon, and François Willaime. 2016. "Plastic Anisotropy and Dislocation Trajectory in BCC Metals." *Nature Communications* 7 (May): 11695.

Dhakal, P, G Ciovati, GR Myneni, KE Gray, N Groll, P Maheshwari, DM McRae, R
    Pike, T Proslier, and F Stevie. 2013. "Effect of High Temperature Heat
    Treatments on the Quality Factor of a Large-Grain Superconducting Radio-
    Frequency Niobium Cavity." *Physical Review Special Topics-Accelerators and
    Beams* 16 (4): 042001.

Dhakal, Pashupati, Santosh Chetri, Shreyas Balachandran, Peter J. Lee, and Gianluigi
    Ciovati. 2018. "Effect of Low Temperature Baking in Nitrogen on the
    Performance of a Niobium Superconducting Radio Frequency Cavity." *Physical
    Review Accelerators and Beams* 21 (3): 032001.

Dhakal, Pashupati, Gianluigi Ciovati, Peter Kneisel, and Ganapati Rao Myneni. 2015.
    "Enhancement in Quality Factor of SRF Niobium Cavities by Material
    Diffusion." *IEEE Transactions on Applied Superconductivity* 25 (3): 1–4.

Dhakal, Pashupati, Gianluigi Ciovati, and Ganapati Rao Myneni. 2012. "A Path to
    Higher Q0 with Large Grain Niobium Cavities." *ArXiv Preprint
    ArXiv:1205.6736.*

———. 2017. "Role of Thermal Resistance on the Performance of Superconducting
    Radio Frequency Cavities." *Physical Review Accelerators and Beams* 20 (3):
    032003.

Domain, Christophe, and Ghiath Monnet. 2005. "Simulation of Screw Dislocation
    Motion in Iron by Molecular Dynamics Simulations." *Physical Review Letters* 95
    (21): 215506. https://doi.org/10.1103/PhysRevLett.95.215506.

Du, Q., V. Faber, and M. Gunzburger. 1999. "Centroidal Voronoi Tessellations:
    Applications and Algorithms." *SIAM Review* 41 (4): 637–76.
    https://doi.org/10.1137/S0036144599352836.

Duesbery, M. S., and V. Vitek. 1998. "Plastic Anisotropy in b.c.c. Transition Metals."
    Acta Materialia 46 (5): 1481–92. https://doi.org/10.1016/S1359-6454(97)00367-
    4.

Duesbery, M. S., V. Vitek, and D. K. Bowen. 1973. "The Effect of Shear Stress on the
    Screw Dislocation Core Structure in Body-Centred Cubic Lattices." *Proceedings
    of the Royal Society of London A: Mathematical, Physical and Engineering
    Sciences* 332 (1588): 85–111. https://doi.org/10.1098/rspa.1973.0014.

Faber, K., and H. Schultz. 1972. "Hydrogen Contamination in Tantalum and Niobium
    Following UHV-Degassing." *Scripta Metallurgica* 6 (11): 1065–70.
    https://doi.org/10.1016/0036-9748(72)90188-3.

Fellinger, Michael R., Hyoungki Park, and John W. Wilkins. 2010. "Force-Matched Embedded-Atom Method Potential for Niobium." *Physical Review B* 81 (14): 144119. https://doi.org/10.1103/PhysRevB.81.144119.

Ford, Denise C, Lance D Cooley, and David N Seidman. 2013a. "Suppression of Hydride Precipitates in Niobium Superconducting Radio-Frequency Cavities." *Superconductor Science and Technology* 26 (10): 105003.

———. 2013b. "First-Principles Calculations of Niobium Hydride Formation in Superconducting Radio-Frequency Cavities." *Superconductor Science and Technology* 26 (9): 095002. https://doi.org/10.1088/0953-2048/26/9/095002.

Ford, Denise C., Peter Zapol, and Lance D. Cooley. 2015. "First-Principles Study of Carbon and Vacancy Structures in Niobium." *The Journal of Physical Chemistry C* 119 (26): 14728–36. https://doi.org/10.1021/acs.jpcc.5b00372.

Frederiksen, Søren L., and Karsten W. Jacobsen. 2003. "Density Functional Theory Studies of Screw Dislocation Core Structures in Bcc Metals." *Philosophical Magazine* 83 (3): 365–75. https://doi.org/10.1080/0141861021000034568.

G. Lucovsky, C. C. Fulton, Y. Zhang, Y. Zou, J. Luning, L. F. Edge, J. L. Whitten, et al. 2005. "Conduction Band-Edge States Associated with the Removal of d-State Degeneracies by the Jahn-Teller Effect." *IEEE Transactions on Device and Materials Reliability* 5 (1): 65–83. https://doi.org/10.1109/TDMR.2005.845804.

G Pfeiffer and H Wipf. 1976. "The Trapping of Hydrogen in Niobium by Nitrogen Interstitials." *Journal of Physics F: Metal Physics* 6 (2): 167.

Garg, P., I. Adlakha, and K. N. Solanki. 2019. "First-Principles Investigation of the Effect of Solutes on the Ideal Shear Resistance and Electronic Properties of Magnesium." In *Magnesium Technology 2019*, edited by Vineet V. Joshi, J. Brian Jordon, Dmytro Orlov, and Neale R. Neelameggham, 231–37. Springer International Publishing.

Garg, P., I. Adlakha, and K.N. Solanki. 2018. "Effect of Solutes on Ideal Shear Resistance and Electronic Properties of Magnesium: A First-Principles Study." *Acta Materialia* 153 (July): 327–35. https://doi.org/10.1016/j.actamat.2018.05.014.

Garg, P., S. Balachandran, I. Adlakha, P. J. Lee, T. R. Bieler, and K. N. Solanki. 2018. "Revealing the Role of Nitrogen on Hydride Nucleation and Stability in Pure Niobium Using First-Principles Calculations." *Superconductor Science and Technology* 31 (11): 115007.

Garg, P., M. A. Bhatia, S. N. Mathaudhu, and K. N. Solanki. 2017. "Solute Effect on Strength and Formability of Mg: A First-Principle Study." In *Magnesium Technology 2017*, edited by Kiran N. Solanki, Dmytro Orlov, Alok Singh, and Neale R. Neelameggham, 483–89. Springer International Publishing.

Garg, P., M.A. Bhatia, and K.N. Solanki. 2019. "Uncovering the Influence of Metallic and Non-Metallic Impurities on the Ideal Shear Strength and Ductility of Ti: An Ab-Initio Study." *Journal of Alloys and Compounds* 788 (June): 413–21. https://doi.org/10.1016/j.jallcom.2019.02.231.

Garg, Pulkit, Ilaksh Adlakha, Shreyas Balachandran, Thomas Bieler, Peter Lee, and Kiran Solanki. 2018. "Role of Nitrogen on Hydride Nucleation in Pure Niobium by First Principles Calculations." In , 741–45. JACOW, Geneva, Switzerland.

Gonnella, Dan, Mingqi Ge, Fumio Furuta, and Matthias Liepe. 2014. "Nitrogen Treated Cavity Testing at Cornell." In .

Gonnella, Dan, John Kaufman, and Matthias Liepe. 2016. "Impact of Nitrogen Doping of Niobium Superconducting Cavities on the Sensitivity of Surface Resistance to Trapped Magnetic Flux." *Journal of Applied Physics* 119 (7): 073904. https://doi.org/10.1063/1.4941944.

Gonnella, Dan, and Matthias Liepe. 2014. "New Insights into Heat Treatment of SRF Cavities in a Low-Pressure Nitrogen Atmosphere." *Proceedings of IPAC* 14: 2634–37.

Gordon, P.A., T. Neeraj, and M.I. Mendelev. 2011. "Screw Dislocation Mobility in BCC Metals: A Refined Potential Description for α-Fe." *Philosophical Magazine* 91 (30): 3931–45. https://doi.org/10.1080/14786435.2011.597947.

Grad, G. B., P. Blaha, J. Luitz, K. Schwarz, A. Fernández Guillermet, and S. J. Sferco. 2000. "Electronic Structure and Chemical Bonding Effects upon the Bcc to $\ensuremath{\Omega}$ Phase Transition: Ab Initio Study of Y, Zr, Nb, and Mo." *Physical Review B* 62 (19): 12743–53. https://doi.org/10.1103/PhysRevB.62.12743.

Gröger, R, and V Vitek. 2012. "Constrained Nudged Elastic Band Calculation of the Peierls Barrier with Atomic Relaxations." *Modelling and Simulation in Materials Science and Engineering* 20 (3): 035019. https://doi.org/10.1088/0965-0393/20/3/035019.

Gupta, Michèle. 1982. "Electronic Properties and Electron-Phonon Coupling in Zirconium and Niobium Hydrides." *Physical Review B* 25 (2): 1027–38.

Gurevich, A., and G. Ciovati. 2013. "Effect of Vortex Hotspots on the Radio-Frequency Surface Resistance of Superconductors." *Physical Review B* 87 (5): 054502. https://doi.org/10.1103/PhysRevB.87.054502.

Gurevich, Alex. 2012. "Superconducting Radio-Frequency Fundamentals for Particle Accelerators." *Reviews of Accelerator Science and Technology* 5: 119–46.

Hardie, D, and P McIntyre. 1973. "The Low-Temperature Embrittlement of Niobium and Vanadium by Both Dissolved and Precipitated Hydrogen." *Metallurgical and Materials Transactions B* 4 (5): 1247–54.

Henkelman, Graeme, and Hannes Jónsson. 2000. "Improved Tangent Estimate in the Nudged Elastic Band Method for Finding Minimum Energy Paths and Saddle Points." *The Journal of Chemical Physics* 113 (22): 9978–85. https://doi.org/10.1063/1.1323224.

Higuchi, T, K Saito, Y Yamazaki, T Ikeda, and S Ohgushi. 2001. "Proceeding. of the 10th Workshop on RF Superconductivity." *Tsukuba, Japan*, 279.

Hirth, J. P., and J. Lothe. 1966. *Dislocation Theory*. McGraw-Hill.

Huang, Shichun, Takayuki Kubo, and RL Geng. 2016. "Dependence of Trapped-Flux-Induced Surface Resistance of a Large-Grain Nb Superconducting Radio-Frequency Cavity on Spatial Temperature Gradient during Cooldown through T c." *Physical Review Accelerators and Beams* 19 (8): 082001.

Isagawa, S. 1980. "Hydrogen Absorption and Its Effect on Low-temperature Electric Properties of Niobium." *Journal of Applied Physics* 51 (8): 4460–70. https://doi.org/10.1063/1.328267.

Itakura, M., H. Kaburaki, and M. Yamaguchi. 2012a. "First-Principles Study on the Mobility of Screw Dislocations in Bcc Iron." *Acta Materialia* 60 (9): 3698–3710. https://doi.org/10.1016/j.actamat.2012.03.033.

———. 2012b. "First-Principles Study on the Mobility of Screw Dislocations in Bcc Iron." *Acta Materialia* 60 (9): 3698–3710. https://doi.org/10.1016/j.actamat.2012.03.033.

Ito, K., and V. Vitek. 2001. "Atomistic Study of Non-Schmid Effects in the Plastic Yielding of Bcc Metals." *Philosophical Magazine A* 81 (5): 1387–1407. https://doi.org/10.1080/01418610108214447.

Jani, A. R., N. E. Brener, and J. Callaway. 1988. "Band Structure and Related Properties of Bcc Niobium." *Physical Review B* 38 (14): 9425–33. https://doi.org/10.1103/PhysRevB.38.9425.

Janisch, Rebecca, and Christian Elsässer. 2003. "Segregated Light Elements at Grain Boundaries in Niobium and Molybdenum." *Physical Review B* 67 (22). https://doi.org/10.1103/PhysRevB.67.224101.

Jin, Hyungyu, Oscar D. Restrepo, Nikolas Antolin, Stephen R. Boona, Wolfgang Windl, Roberto C. Myers, and Joseph P. Heremans. 2015. "Phonon-Induced Diamagnetic Force and Its Effect on the Lattice Thermal Conductivity." *Nat Mater* 14 (6): 601–6.

Jisrawi, N. M., M. W. Ruckman, T. R. Thurston, G. Reisfeld, M. Weinert, M. Strongin, and M. Gurvitch. 1998. "Reversible Depression in the T c of Thin Nb Films Due to Enhanced Hydrogen Adsorption." *Physical Review B* 58 (10): 6585.

Khanra, BC. 1975. "Flux Pinning by Grain Boundaries in Anisotropic Superconducting Materials." *Physica Status Solidi (b)* 72 (1): 303–8.

Kim, Yoon-Jun, Runzhe Tao, Robert F. Klie, and David N. Seidman. 2013. "Direct Atomic-Scale Imaging of Hydrogen and Oxygen Interstitials in Pure Niobium Using Atom-Probe Tomography and Aberration-Corrected Scanning Transmission Electron Microscopy." *ACS Nano* 7 (1): 732–39. https://doi.org/10.1021/nn305029b.

Knobloch, J. 2003. "The 'Q Disease' in Superconducting Niobium RF Cavities." In , 671:133–50. AIP. https://doi.org/10.1063/1.1597364.

Knobloch, J, and H Padamsee. 1997. "Flux Trapping in Niobium Cavities during Breakdown Events." In , 337.

Korhonen, T., M. J. Puska, and R. M. Nieminen. 1995. "Vacancy-Formation Energies for Fcc and Bcc Transition Metals." *Physical Review B* 51 (15): 9526–32. https://doi.org/10.1103/PhysRevB.51.9526.

Korzhavyi, P. A., I. A. Abrikosov, B. Johansson, A. V. Ruban, and H. L. Skriver. 1999. "First-Principles Calculations of the Vacancy Formation Energy in Transition and Noble Metals." *Physical Review B* 59 (18): 11693–703. https://doi.org/10.1103/PhysRevB.59.11693.

Kresse, G., and J. Hafner. 1994. "Norm-Conserving and Ultrasoft Pseudopotentials for First-Row and Transition Elements." *Journal of Physics: Condensed Matter* 6 (40): 8245.

Kresse, Georg, and Jürgen Furthmüller. 1996. "Efficient Iterative Schemes for Ab Initio Total-Energy Calculations Using a Plane-Wave Basis Set." *Physical Review B* 54 (16): 11169.

Kresse, Georg, and Jürgen Hafner. 1993. "Ab Initio Molecular Dynamics for Liquid Metals." *Physical Review B* 47 (1): 558.

Kubo, Takayuki. 2016. "Flux Trapping in Superconducting Accelerating Cavities during Cooling down with a Spatial Temperature Gradient." *Progress of Theoretical and Experimental Physics* 2016 (5).

Lagos, M., G. Martinez, and Ivan K. Schuller. 1984. "Kinetics of Hydrogen Absorption in Transition Metals and Subsurface Bonding." *Physical Review B* 29 (10): 5979–81.

Lee, PJ, AA Polyanskii, A Gurevich, AA Squitieri, David C Larbalestier, PC Bauer, C Boffo, and HT Edwards. 2006. "Grain Boundary Flux Penetration and Resistivity in Large Grain Niobium Sheet." *Physica C: Superconductivity* 441 (1–2): 126–29.

Lee, P.J., A.A. Polyanskii, A. Gurevich, A.A. Squitieri, D.C. Larbalestier, P.C. Bauer, C. Boffo, and H.T. Edwards. 2006. "Grain Boundary Flux Penetration and Resistivity in Large Grain Niobium Sheet." *Proceedings of the 12th International Workshop on RF Superconductivity* 441 (1): 126–29. https://doi.org/10.1016/j.physc.2006.03.027.

Lu, Wei, AnYuan Gao, YueLin Liu, and ZhenHong Dai. 2012. "Diffusion Behaviors of Hydrogen Isotopes in Niobium from First-Principles." *Science China Physics, Mechanics and Astronomy* 55 (12): 2378–82. https://doi.org/10.1007/s11433-012-4933-0.

Martinello, M., A. Grassellino, M. Checchin, A. Romanenko, O. Melnychuk, D. A. Sergatskov, S. Posen, and J. F. Zasadzinski. 2016. "Effect of Interstitial Impurities on the Field Dependent Microwave Surface Resistance of Niobium." *Applied Physics Letters* 109 (6): 062601. https://doi.org/10.1063/1.4960801.

Matsushita, Teruo. 2007. *Flux Pinning in Superconductors*. Vol. 164. Springer.

Mattsson, Thomas R., and Ann E. Mattsson. 2002. "Calculating the Vacancy Formation Energy in Metals: Pt, Pd, and Mo." *Physical Review B* 66 (21): 214110. https://doi.org/10.1103/PhysRevB.66.214110.

Meissner, W., and R. Ochsenfeld. 1933. "Ein Neuer Effekt Bei Eintritt Der Supraleitfähigkeit." *Naturwissenschaften* 21 (44): 787–88. https://doi.org/10.1007/BF01504252.

Millett, Paul C, Tapan Desai, Vesselin Yamakov, and Dieter Wolf. 2008. "Atomistic Simulations of Diffusional Creep in a Nanocrystalline Body-Centered Cubic Material." *Acta Materialia* 56 (14): 3688–98.

Momma, Koichi, and Fujio Izumi. 2008. "*VESTA* : A Three-Dimensional Visualization System for Electronic and Structural Analysis." *Journal of Applied Crystallography* 41 (3): 653–58. https://doi.org/10.1107/S0021889808012016.

Monkhorst, Hendrik J., and James D. Pack. 1976. "Special Points for Brillouin-Zone Integrations." *Phys. Rev. B* 13 (12): 5188–5192. https://doi.org/10.1103/PhysRevB.13.5188.

Moruzzi, V. L., and P. M. Marcus. 1990. "Antiferromagnetism in 4d Transition Metals." *Physical Review B* 42 (16): 10322–28. https://doi.org/10.1103/PhysRevB.42.10322.

Myers, S. M., M. I. Baskes, H. K. Birnbaum, J. W. Corbett, G. G. DeLeo, S. K. Estreicher, E. E. Haller, et al. 1992. "Hydrogen Interactions with Defects in Crystalline Solids." *Reviews of Modern Physics* 64 (2): 559–617.

Narlikar, AV, and D Dew-Hughes. 1964. "The Effect of Dislocation Configuration on the Superconducting Properties of Niobium and Vanadium." *Physica Status Solidi (b)* 6 (2): 383–90.

Pande, CS, and M Suenaga. 1976. "A Model of Flux Pinning by Grain Boundaries in Type-II Superconductors." *Applied Physics Letters* 29 (7): 443–44.

Peter, F, M Muck, and C Heiden. 1993. "Highly Textured Niobium Films for Applications in Vortex-Electronics." *IEEE Transactions on Applied Superconductivity* 3 (1): 2968–71.

Plimpton, Steve. 1995. "Fast Parallel Algorithms for Short-Range Molecular Dynamics." *Journal of Computational Physics* 117 (1): 1–19.

Pronsato, M Estela, Carolina Pistonesi, and Alfredo Juan. 2004. "Density Functional Study of H–Fe Vacancy Interaction in Bcc Iron." *Journal of Physics: Condensed Matter* 16 (39): 6907–16. https://doi.org/10.1088/0953-8984/16/39/023.

Rajagopalan, M., I. Adlakha, M. A. Tschopp, and K. N. Solanki. 2017. "Energetics of Hydrogen Segregation to α-Fe Grain Boundaries for Modeling Stress Corrosion Cracking." *JOM* 69 (8): 1398–1403. https://doi.org/10.1007/s11837-017-2386-7.

Rajagopalan, M., M.A. Bhatia, M.A. Tschopp, D.J. Srolovitz, and K.N. Solanki. 2014. "Atomic-Scale Analysis of Liquid-Gallium Embrittlement of Aluminum Grain Boundaries." *Acta Materialia* 73 (July): 312–25. https://doi.org/10.1016/j.actamat.2014.04.011.

Rajagopalan, M., M. A. Tschopp, and K. N. Solanki. 2014. "Grain Boundary Segregation of Interstitial and Substitutional Impurity Atoms in Alpha-Iron." *JOM* 66 (1): 129–38. https://doi.org/10.1007/s11837-013-0807-9.

Ramasubramaniam, Ashwin, Mitsuhiro Itakura, and Emily A. Carter. 2009. "Interatomic Potentials for Hydrogen in α–Iron Based on Density Functional Theory." *Physical Review B* 79 (17): 174101.

Rice, James R, and Jian-Sheng Wang. 1989. "Embrittlement of Interfaces by Solute Segregation." *Materials Science and Engineering: A* 107: 23–40.

Ricker, RE, and GR Myneni. 2010. "Evaluation of the Propensity of Niobium to Absorb Hydrogen during Fabrication of Superconducting Radio Frequency Cavities for Particle Accelerators." *Journal of Research of the National Institute of Standards and Technology* 115 (5): 353.

Rittner, J. D., and D. N. Seidman. 1996. " 〈110〉 Symmetric Tilt Grain-Boundary Structures in Fcc Metals with Low Stacking-Fault Energies." *Physical Review B* 54 (10): 6999–7015. https://doi.org/10.1103/PhysRevB.54.6999.

Rodney, D., L. Ventelon, E. Clouet, L. Pizzagalli, and F. Willaime. 2017. "Ab Initio Modeling of Dislocation Core Properties in Metals and Semiconductors." *Acta Materialia* 124 (February): 633–59. https://doi.org/10.1016/j.actamat.2016.09.049.

Romanenko, A, F Barkov, L D Cooley, and A Grassellino. 2013. "Proximity Breakdown of Hydrides in Superconducting Niobium Cavities." *Superconductor Science and Technology* 26 (3): 035003. https://doi.org/10.1088/0953-2048/26/3/035003.

Romero, Aldo H., Ivan K. Schuller, and Ricardo Ramirez. 1998. "Subsurface Bonding of Hydrogen in Niobium: A Molecular-Dynamics Study." *Physical Review B* 58 (23): 15904–8.

Sadananda, K, and AK Vasudevan. 2011. "Review of Environmentally Assisted Cracking." *Metallurgical and Materials Transactions A* 42 (2): 279–95.

Sanville, Edward, Steven D Kenny, Roger Smith, and Graeme Henkelman. 2007. "Improved Grid-based Algorithm for Bader Charge Allocation." *Journal of Computational Chemistry* 28 (5): 899–908.

Schober, T., M. A. Pick, and H. Wenzl. 1973. "Electron Microscopy of β-Hydride in Niobium." *Physica Status Solidi (a)* 18 (1): 175–182. https://doi.org/10.1002/pssa.2210180114.

Sharma, S., J. K. Dewhurst, C. Ambrosch-Draxl, S. Kurth, N. Helbig, S. Pittalis, S. Shallcross, L. Nordström, and E. K. U. Gross. 2007. "First-Principles Approach to Noncollinear Magnetism: Towards Spin Dynamics." *Physical Review Letters* 98 (19): 196405.

Sharma, S., S. Pittalis, S. Kurth, S. Shallcross, J. K. Dewhurst, and E. K. U. Gross. 2007. "Comparison of Exact-Exchange Calculations for Solids in Current-Spin-Density- and Spin-Density-Functional Theory." *Physical Review B* 76 (10): 100401.

Singh, Divya, and Avinash Parashar. 2018. "Effect of Symmetric and Asymmetric Tilt Grain Boundaries on the Tensile Behaviour of Bcc-Niobium." *Computational Materials Science* 143 (February): 126–32. https://doi.org/10.1016/j.commatsci.2017.11.005.

Smith, R. J. 1980. "Characterization of the Hydrogen Adsorption/Absorption Process for Nb(110) with Surface Spectroscopy." *Physical Review Letters* 45 (15): 1277–80.

Solanki, Kiran N., Mark A. Tschopp, Mehul A. Bhatia, and Nathan R. Rhodes. 2013. "Atomistic Investigation of the Role of Grain Boundary Structure on Hydrogen Segregation and Embrittlement in α-Fe." *Metallurgical and Materials Transactions A* 44 (3): 1365–75. https://doi.org/10.1007/s11661-012-1430-z.

Stroh, AN. 1958. "Dislocations and Cracks in Anisotropic Elasticity." *Philosophical Magazine* 3 (30): 625–46.

Sung, Z.-H., M. Wang, A. A. Polyanskii, C. Santosh, S. Balachandran, C. Compton, D. C. Larbalestier, T. R. Bieler, and P. J. Lee. 2017. "Development of Low Angle Grain Boundaries in Lightly Deformed Superconducting Niobium and Their Influence on Hydride Distribution and Flux Perturbation." *Journal of Applied Physics* 121 (19): 193903. https://doi.org/10.1063/1.4983512.

Tao, R., A. Romanenko, L. D. Cooley, and R. F. Klie. 2013. "Low Temperature Study of Structural Phase Transitions in Niobium Hydrides." *Journal of Applied Physics* 114 (4): 044306. https://doi.org/10.1063/1.4816274.

Trenikhina, Y., A. Romanenko, J. Kwon, J.-M. Zuo, and J. F. Zasadzinski. 2015. "Nanostructural Features Degrading the Performance of Superconducting Radio Frequency Niobium Cavities Revealed by Transmission Electron Microscopy and Electron Energy Loss Spectroscopy." *Journal of Applied Physics* 117 (15): 154507.

Tschopp, M. A., K. N. Solanki, F. Gao, X. Sun, M. A. Khaleel, and M. F. Horstemeyer. 2012. "Probing Grain Boundary Sink Strength at the Nanoscale: Energetics and Length Scales of Vacancy and Interstitial Absorption by Grain Boundaries in $\ensuremath{\alpha}$-Fe." *Physical Review B* 85 (6): 064108. https://doi.org/10.1103/PhysRevB.85.064108.

Ullmaier, H, K Papastaikoudis, S Takacs, and W Schilling. 1970. "Pinning of Flux Lines in Superconducting Niobium Due to Point Defects." *Physica Status Solidi (b)* 41 (2): 671–79.

Vallet, C, M Boloré, B Bonin, JP Charrier, B Daillant, J Gratadour, F Koechlin, and H Safa. 1992. "Flux Trapping in Superconducting Cavities." In , 1295.

Ventelon, Lisa, B. Lüthi, E. Clouet, L. Proville, B. Legrand, D. Rodney, and F. Willaime. 2015. "Dislocation Core Reconstruction Induced by Carbon Segregation in Bcc Iron." *Physical Review B* 91 (22): 220102. https://doi.org/10.1103/PhysRevB.91.220102.

Ventelon, Lisa, F. Willaime, E. Clouet, and D. Rodney. 2013. "Ab Initio Investigation of the Peierls Potential of Screw Dislocations in Bcc Fe and W." *Acta Materialia* 61 (11): 3973–85. https://doi.org/10.1016/j.actamat.2013.03.012.

Vinnikov, L, EA Zasavitskii, and SI Moskvin. 1982. "Critical Currents in Niobium Bicrystals." *Zh. Eksp. Teor. Fiz.* 83 (6): 2225–36.

Vitek †, V. 2004. "Core Structure of Screw Dislocations in Body-Centred Cubic Metals: Relation to Symmetry and Interatomic Bonding." *Philosophical Magazine* 84 (3–5): 415–28. https://doi.org/10.1080/14786430310001611644.

Vitek, V., and V. Paidar. 2008. "Chapter 87 - Non-Planar Dislocation Cores: A Ubiquitous Phenomenon Affecting Mechanical Properties of Crystalline Materials." In *Dislocations in Solids*, edited by J. P. Hirth, 14:439–514. A Tribute to F.R.N. Nabarro. Elsevier. http://www.sciencedirect.com/science/article/pii/S1572485907000071.

Vitek, V, RC Perrin, and DK Bowen. 1970. "The Core Structure of ½ (111) Screw Dislocations in Bcc Crystals." *Philosophical Magazine* 21 (173): 1049–73.

Vitek, Vo. 1974. "Theory of the Core Structures of Dislocations in BCC Metals." *Cryst. Lattice Defects* 5 (1): 1–34.

Wachowicz, E, and A Kiejna. 2008. "Effect of Impurities on Grain Boundary Cohesion in Bcc Iron." *Computational Materials Science* 43 (4): 736–43.

Watanabe, T., S. Tsurekawa, X. Zhao, and L. Zuo. 2006. "Grain Boundary Engineering by Magnetic Field Application." *Viewpoint Set No. 40: Grain Boundary Engineering* 54 (6): 969–75. https://doi.org/10.1016/j.scriptamat.2005.11.036.

Weinberger, Christopher R., Garritt J. Tucker, and Stephen M. Foiles. 2013. "Peierls Potential of Screw Dislocations in Bcc Transition Metals: Predictions from Density Functional Theory." *Physical Review B* 87 (5): 054114. https://doi.org/10.1103/PhysRevB.87.054114.

Welter, J. -M., and F. J. Johnen. 1977. "Superconducting Transition Temperature and Low Temperature Resistivity in the Niobium-Hydrogen System." *Zeitschrift Für Physik B Condensed Matter* 27 (3): 227–32. https://doi.org/10.1007/BF01325532.

Wildes, AR, J Mayer, and K Theis-Bröhl. 2001. "The Growth and Structure of Epitaxial Niobium on Sapphire." *Thin Solid Films* 401 (1–2): 7–34.

Wolverton, C. 2007. "Solute–Vacancy Binding in Aluminum." *Acta Materialia* 55 (17): 5867–72. https://doi.org/10.1016/j.actamat.2007.06.039.

Yamaguchi, Masatake, Ken-Ichi Ebihara, Mitsuhiro Itakura, Tomoko Kadoyoshi, Tomoaki Suzudo, and Hideo Kaburaki. 2011. "First-Principles Study on the Grain Boundary Embrittlement of Metals by Solute Segregation: Part II. Metal (Fe, Al, Cu)-Hydrogen (H) Systems." *Metallurgical and Materials Transactions A* 42 (2): 330–39.

Yamaguchi, Masatake, Motoyuki Shiga, and Hideo Kaburaki. 2004. "First-Principles Study on Segregation Energy and Embrittling Potency of Hydrogen in Niσ5 (012) Tilt Grain Boundary." *Journal of the Physical Society of Japan* 73 (2): 441–49.

Yang, Jia-Yue, Sheng-Ying Yue, and Ming Hu. 2016. "Bidirectional Effect of Magnetic Field on Electronic Thermal Transport of Metals from All-Electron First-Principles Calculations." *Physical Review B* 94 (23). https://doi.org/10.1103/PhysRevB.94.235153.

Zhao, Yi, and Gang Lu. 2011. "QM/MM Study of Dislocation—Hydrogen/Helium Interactions in α-Fe." *Modelling and Simulation in Materials Science and Engineering* 19 (6): 065004.

APPENDIX A

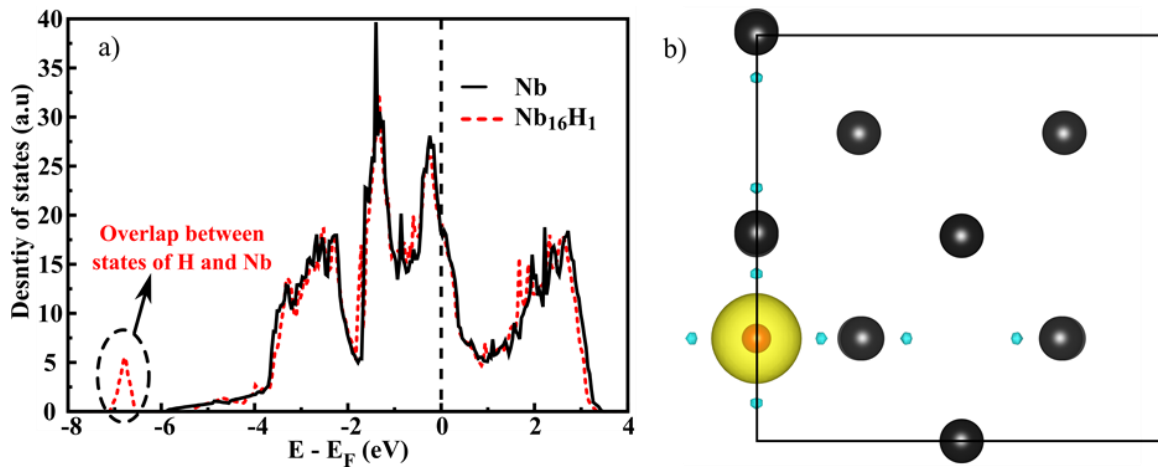ELECTRONIC STRUCTURE CALCULATIONS FOR INTERSTITAL HYDROGEN

IN NIOBIUM

Figure A1: (a) Total density of state and (b) valence charge transfer contours for $Nb_{16}H_1$ (hydrogen atom at a tetrahedral site). Yellow and cyan iso-charge surfaces respectively represent an accumulation and depletion of charge of $0.027e/\text{Å}^3$ in (b).

APPENDIX B

NUMBER OF ATOMS AND K-POINT MESH USED FOR GRAIN BOUNDARIES

Table A1: Number of atoms in the simulation cell and the k-point mesh used for different grain boundaries.

Grain Boundary	Atoms	K-point mesh
Σ5 (210)	60	6 x 1 x 14
Σ5 (310)	84	4 x 1 x 14
Σ13 (023)	104	4 x 1 x 14
Σ37 (016)	144	4 x 1 x 9
Σ17 (014)	68	2 x 1 x 9
Σ3 (111)	66	4 x 1 x 7
Σ1 (101)	72	6 x 1 x 14